Theoretical Modeling of Interface Specific Vibrational Spectroscopy: Methods and Applications to Aqueous Interfaces

Angela Perry,† Christine Neipert,† and Brian Space*

Department of Chemistry, University of South Florida, Tampa, Florida 33620-5250

Preston B. Moore

Department of Chemistry and Biochemistry, University of the Sciences in Philadelphia, Philadelphia, Pennsylvania 19104

Received June 17, 2005

Contents

* To whom correspondence should be addressed. Tel: 813-765-4846. Fax: 813-974-3203. E-mail: space@cas.usf.edu.
† In partial fulfillment of the requirements for the Ph.D.—both C.N. and A.P. were the primary graduate student authors and contributed equally to this work.

1. Introduction

Liquid water interfaces are ubiquitous and important in chemistry and the environment. Thus, with the advent of interface specific nonlinear optical spectroscopies, such interfaces have been intensely studied—both theoretically[1−15] and experimentally.[16−43] Sum frequency generation (SFG) spectroscopy is a powerful experimental method for probing the structure and dynamics of interfaces. SFG is a second-order polarization experiment, and the more common electronically nonresonant experiment is the main focus of this review (although the theory of other second-order processes is discussed). SFG spectroscopy is dipole forbidden in centrosymmetric media—such as liquids. Interfaces serve to break the isotropic symmetry and produce a dipolar second-order signal that is sensitive only to the interface in most cases. Contributions from the bulk allowed quadrupolar effects have been demonstrated to be negligible in some cases[44,45] but can be included if necessary,[13] and in that case, contributions from the bulk and interface are obtained in the sum frequency signal. The SFG experiment typically employs both a visible and an infrared (IR) laser field overlapping in time and space at the interface and can be performed in the time or frequency domain.[16,22,46−53] In the absence of any vibrational resonance at the instantaneous IR laser frequency, a structureless signal due to the static hyperpolarizability of the interface is obtained.[4,19,25] When the IR laser frequency is in tune with a vibration at the interface, a resonant line shape is obtained with a characteristic shape that reflects both the structural and the dynamical environment at the interface.[2,14,54]

Recent years have seen a great increase in the number of experimental groups performing SFG investigations. In contrast, molecularly detailed theoretical simulations of SFG spectra are comparatively few and have only recently begun making a significant impact. Like all vibrational spectroscopies, the goal of SFG spectroscopy is to infer structural and dynamical properties from the observed spectroscopic signatures. In contrast to more traditional vibrational spectroscopies, SFG line shapes tend to be more complex (reflecting the unique environment that is present at an interfacial boundary) and are not nearly as well understood. Thus, the advent of effective theoretical simulation techniques promises to help realize the potential of SFG spectroscopy to permit detailed characterization of interfaces on par with that done in the bulk. Furthermore, in analogy

10.1021/cr040379y CCC: $59.00
Published on Web 02/24/2006

Angela Perry is an Assistant Professor of Chemistry at the University of Tampa. She received her Ph.D. degree under the mentorship of Professor Brian Space at the University of South Florida in 2005. Angela was the recipient of several awards, honors, and scholarships prior to and during graduate school. She chaired the Castle Research Conference at the University of South Florida where graduate and undergraduate students presented their research. During her final 2 years in graduate school, she was a National Science Foundation-funded Research Assistant focusing on research and mentoring within the Space group. Angela has authored several important papers studying the spectroscopic properties of interfaces. Accurately describing condensed phase spectroscopy is difficult theoretically; however, the work she has contributed to leads to interesting new theory and crucial insights into the information content inherent in empirical line shapes. Angela is currently starting a research group at the University of Tampa with undergraduates to theoretically describe the SFG spectroscopy of more complex systems.

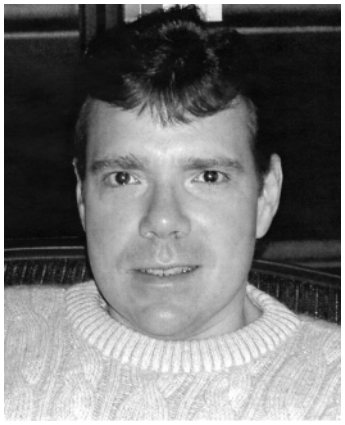

Brian Space is a Professor of Chemistry at the University of South Florida. He received his Ph.D. under the mentorship of David Coker at Boston University in 1992. He was then a National Science Foundation, Computational Science and Engineering Postdoctoral Research Associate with Professor Herschel Rabitz at Princeton University for 3 years. From 1995 to 2000, he was a faculty member at Duquesne University before moving to the University of South Florida as an Associate Professor in 2000; in 1998, he received an NSF Career Award. The Space group is known for constructing molecularly detailed dynamics simulation methods. Their recent work has uncovered the fact that high frequency, ostensibly quantum mechanical, nonlinear spectroscopic line shapes are frequently well-described by a single classical TCF—a surprising result that represents a major simplification.

Christine Neipert graduated with her B.S. in Chemistry from Maryville University in Saint Louis, Missouri, where she received several awards and scholarships—including the National Institute of Chemists award. As an undergraduate, she conducted research in physical chemistry under the mentorship of Dr. Gary Beall. Christine is currently a third year graduate student at the University of South Florida in Dr. Brian Space's research group and is the recipient of the Latino Graduate Fellowship in conjunction with a NSF-funded research assistantship. Her current research focus is on developing computationally amenable theoretical descriptions of nonlinear spectroscopies.

Preston B. Moore is currently a Professor of Chemistry & Biochemistry at the University of the Sciences in Philadelphia (USP) (http://www.usip.edu/chemistry and http://hydrogen.usip.edu/moore). He received his Ph.D. under the mentorship of David Coker at Boston University in 1993. He was a Postdoctoral fellow with Professor Michael Klein at the University of Pennsylvania for 3 years before becoming the associate director for the Center for Molecular Modeling (CMM http://www.cmm.upenn.edu) at the University of Pennsylvania. In 2002, he became a faculty member at the University of the Sciences in Philadelphia. Dr. Moore is known for algorithm development and is the author of the MD code CM3D. He and collaborators use this code to gain detailed insight of molecular interactions and physiochemical properties in systems such as water, liquid CS_2, proteins, and ion channels embedded within biological membranes. Recent work has focused on biological membranes with proteins and liquid/liquid interfaces.

with condensed phase experiments, SFG experiments have recently begun being performed using a variety of time and frequency domain techniques taking advantage of the flexibility inherent in measuring a second-order polarization signal.[24,55,56]

An impediment to progress in interpreting SFG spectra has been the difficulty that the theoretical community can experience in understanding crucial experimental issues inherent in these measurements. Conversely, the theoretical machinery needed to describe a SFG measurement is itself complex and sometimes seemingly far removed from the essence of the experiment. Therefore, the purpose of this review is to give a unified description of the experimental and theoretical considerations that are necessary to describe SFG line shapes theoretically in the context of extant measurements and simulations.

Section 2 presents a general theory of nonlinear polarization starting with the *N*-th-order formulas and specializing to second-order processes. This formalism is needed to theoretically describe certain SFG experiments (especially

time domain measurements) that do not utilize effectively monochromatic fields. Appendix A (section 11) details all of the possible second-order signals that result from a three-wave mixing experiment. Section 3 describes how the general formulas simplify in idealized limits—in which most extant experiments have been performed or interpreted. The resulting expressions derived are those frequently presented in the SFG literature.

Next, we present relevant considerations concerning optical experiments at interfaces including the origin and importance of Fresnel factors and the phenomenological expression for the measured second-order (SFG) intensity in terms of the signal field (section 4). The relationship between the common experimental polarization conditions of the experimental fields (SSP, SPS, PPP, and PSS) and microscopic Cartesian susceptibility tensor elements is also presented. The wave vector and phase matching conditions that need to be satisfied for coherent nonlinear optical experiments are discussed in section 5. Experimental designs, including those other than the common monochromatic frequency domain SFG experiment, are discussed in section 6. Section 6.1 details the innovative method of polarization mapping and how this method helps to resolve spectral features. For experiments performed outside of the monochromatic limit, the formulas presented in section 2 are needed to formally theoretically describe the SFG response for time domain techniques that use spectrally broad femtosecond laser excitation pulses. A brief discussion of the experimental results from such SFG measurements is presented in section 6.2.

Next, section 7 presents formal expressions for dipolar (section 7.1), quadrupolar (section 7.2), and static field-induced third-order contributions (section 7.3) to the sum frequency signal. The microscopic formulas for the dipolar and quadrupolar SFG susceptibility tensors are also presented along with a discussion of the rotating wave approximation (RWA) in this context. These expressions provide the tie between the earlier phenomenological expression and the formulas needed to relate a systems dynamics to an SFG signal.

Section 8 discusses theoretical simulations and their results with a focus on aqueous interfaces; comparison with experiment is stressed. Section 8.1 presents a frequency domain approach to calculating SFG signals that represented the first attempt to directly model an SFG signal from a liquid interface. It also discusses other applications of this frequency domain approach. Section 8.2 discusses time domain approaches to calculating SFG spectra including applications to the water/vapor and saltwater/vapor interfaces. Results, including the identification of novel species at the water/vapor interface, are presented. Section 9 presents conclusions and a brief discussion of future directions for theoretical studies of SFG spectroscopy.

2. Theory of the Nonlinear Polarization

SFG experiments are also referred to by terms such as sum frequency vibrational spectroscopy[16,22] to distinguish interfacial electronically nonresonant IR-visible experiments from other SFG experiments.[24,57] For example, recent experiments that are doubly, both electronically and vibrationally, resonant have been performed.[58] SFG experiments measure a second-order polarization generated coherently in a direction given by the experimental wave vector and phase matching conditions.[24,55,57] It is one of several second-order processes that are possible when two applied fields interact with a medium. While the formalism presented here is more general, we will focus on SFG experiments in our presentation and will explicitly state when another second-order process is being discussed. Such measurements are interface specific because even order polarization generating terms are forbidden in centrosymmetric media. This can be understood by considering reversing the direction of all of the fields in an experiment for an isotropic system. Doing so must change the sign of the polarization because all directions are equivalent on average.[57] However, even numbers of fields will make the polarization equal to its negative—a condition that insists that the polarization is zero, i.e., $\mathbf{P} = -\mathbf{P} = 0$.[55] At an interface, or in certain noncentrosymmetric solids,[24] the isotropy of the system is broken. This leads to a second-order signal within the dipole approximation, and in this case, the signal is proportional to the product of the susceptibility and the applied fields as described below.

It should also be noted, even in centrosymmetric media, that bulk quadrupolar contributions to SFG signals are possible but have been shown to be negligible in most cases involving liquid interfaces in the common SFG reflected geometry.[44,45,53,59] (When light impinges on an interface, a SFG signal is generated. This signal is both reflected from the boundary and transmitted through the interface.)[60] They can, however, be important for experiments performed in the transmission geometry.[45] In the case of bulk quadrupoles, their contribution to the second-order signal is proportional to derivatives of the field, which invalidates the above symmetry argument. Molecular dynamics (MD) simulations of the SFG signal, including both bulk and surface terms, represent an excellent mechanism to test the importance of such contributions[13,44] but have not been conducted as of yet.

Like all nonlinear optical experiments, both time and frequency domain approaches to SFG are possible.[46,55] To date, most SFG experiments have been performed in the frequency domain and, effectively, in the limit of monochromatic fields.[16,22,50−53] However, there is growing interest in using both time domain, mixed time, and frequency domain approaches,[46−49] as well as other second-order processes such as difference frequency generation (DFG) spectroscopy.[61−64] The theoretical methods, which will be discussed below, are capable of describing any of these second-order processes. Thus, before specializing the theoretical expressions to the typical monochromatic frequency domain experiment, it is helpful to examine the formal theoretical structure of second-order nonlinear processes. The resulting expressions will be required in calculating signals from experiments outside of the frequency monochromatic or time impulsive limit, e.g., typical time domain experiments. Such experiments are becoming increasingly more common because they can provide, in principle, information distinct from ideal frequency domain experiments.[47] Furthermore, in the final analysis, it is often possible to model SFG experiments without reference to the detailed nature of the experimental measurement. However, there is often confusion in the theoretical community as to what experimental considerations are relevant, and conversely, the theoretical methods may seem opaque and out of context to the experimental community. Thus, we seek to present the methods in a context that adds clarity for both communities.

First, considering an N-th-order process (an $N + 1$ wave mixing experiment), a field is applied at time t at position $\mathbf{r}$ and can be written as:

$$\mathbf{E}(\mathbf{r}, t) = \sum_{n}^{N} [\mathbf{E}_n(\mathbf{t})\, e^{i\mathbf{k_n}\cdot\mathbf{r}} + \mathbf{E}_n^*(\mathbf{t})\, e^{-i\mathbf{k_n}\cdot\mathbf{r}}] \quad (1)$$

In eq 1, $\mathbf{k_n}$ is the wave vector specifying the field propagation direction. Equation 1 is partitioned into components that are slowly varying in space and those that are spatially highly oscillatory.[24,55,65] The slowly varying spacial component, $\mathbf{E_n}(t)$, can generally be further decomposed into temporally ($\epsilon_n(t)$) and spatially ($\mathbf{E}_n$) dependent parts.[65] This subsequent separation allows the field to be rewritten in the form:

$$\mathbf{E}(\mathbf{r}, t) = \sum_{n}^{N} [\mathbf{E}_n \epsilon_n(t)\, e^{i\mathbf{k_n}\cdot\mathbf{r}} + \mathbf{E}_n^* \epsilon_n^*(t)\, e^{-i\mathbf{k_n}\cdot\mathbf{r}}] \quad (2)$$

In eqs 1 and 2, the sum on n is included because, in the most general case, exact time ordering of the applied fields cannot be assumed.[55] In practice, experiments in the time domain typically use relatively short pulses that are separated and ordered in time while the frequency domain techniques employ nearly monochromatic laser fields that overlap in time and space—such considerations simplify the required analysis considerably.

Given the field, the observable nonlinear polarization, $\mathbf{P}^{(N)}$ (within the dipole approximation where the response function and susceptibility tensors are independent of $\mathbf{r}$ and $\mathbf{k}$), takes the form of a multiple time integration over the material response function, $\mathbf{R}^{(N)}$, which contains all of the system variables and information to be probed. (The description of the material system in the time domain is described by the response function and is typically referred to as the susceptibility in the frequency domain.):

$$\mathbf{P}^{(N)}(\mathbf{r}, t) = \int_0^\infty \mathrm{d}\tau_1 \cdots \int_0^\infty \mathrm{d}\tau_N\, \mathbf{R}^{(N)}(\tau_1,\cdots,\tau_N) \mid \mathbf{E}(\mathbf{r}, t-\tau_1)\cdots\mathbf{E}(\mathbf{r}, t-\tau_N) \quad (3)$$

In eq 3, the vertical line represents N tensor contractions. In an N-th-order experiment, there are N relevant times, corresponding to the number of $\mathbf{E}(\mathbf{r}, t)$'s in the expression for $\mathbf{P}^{(N)}(\mathbf{r}, t)$ that are each represented by the sum in eqs 1 or 2. Consequently, when exact time ordering of the applied fields cannot be assumed and eq 2 is used to describe the applied fields, a sum of $(2N)^N$ terms determines the N-th-order polarization. The polarization can then be written as:

$$\mathbf{P}^{(N)}(\mathbf{r}, t) = \sum_{s}^{2^N N^N} \mathbf{P}^{(N)}(\mathbf{k_s}, t) = \sum_{s}^{2^N N^N} \mathbf{P}^{(N)}(t)\, e^{i\mathbf{k_s}\cdot\mathbf{r}} \quad (4)$$

In eq 4, $\mathbf{k_s}$ is the sum of the wave vectors associated with the applied fields and represents the direction that the generated signal will propagate. As is shown in Figure 1, considering a second-order experiment probing an interface, after the nonlinear signal is generated, it will interact with the interface producing a reflected and transmitted signal with modified wave vectors (this issue will be discussed in section 5). Note that $\mathbf{P}^{(N)}(\mathbf{k_s}, t)$ is a complex quantity, and it is *one* of the $(2N)^N$ processes that determines the total N-th-order polarization, $\mathbf{P}^{(N)}(\mathbf{r}, t)$. Furthermore, $\mathbf{P}^{(N)}(\mathbf{r}, t)$ is a real quantity and is the sum of all of the $\mathbf{P}^{(N)}(\mathbf{k_s}, t)$ terms (eq 4). However, once a particular $\mathbf{k_s}$ is chosen (e.g., by the experimental geometry), the signal is a complex quantity, and the real and imaginary parts can be measured separately, e.g., in a heterodyne detected experiment.[66]

In principle, the sum of all $(2N)^N$ terms must be evaluated to calculate the total N-th-order polarization. Considering second-order experiments, this leads to 16 distinct contributions that are described in Appendix A (section 11). In practice, the polarization generated for a given experiment is associated with a particular wave vector and phase matching condition. This implies that when the two incident wave vectors add, a second harmonic generation (SHG)/SFG signal is generated and when the two incident wave vectors interact such that the resulting wave vector is equal to their difference, a DFG signal is generated. For surface probing spectroscopies, the direction that the signal (DFG, SFG, and/or SHG) propagates in will be guided by Snell's (linear and nonlinear) refraction and reflection laws in conjunction with the original propagation directions of incident wave vectors, $\mathbf{k}_1$ and $\mathbf{k}_2$. Thus, with the proper experimental setup in which detectors are placed at the appropriate phase matched angle, it is typical to only detect one of the possible second-order nonlinear processes, e.g., SFG or DFG. Phase matching criteria for surface probing spectroscopies will be discussed more throughly in section 5.

Note that as shown in Appendix A (section 11), there are two $\mathbf{P}^{(2)}(\mathbf{k_s}, t)$ in which the incident wave vectors add; that is, $\mathbf{k_s} = \mathbf{k}_1 + \mathbf{k}_2$. (The additional two terms that are classified under SFG in Appendix A (section 11) are complex conjugates of the experimental wave vectors and contribute to $\mathbf{P}^{(2)}_{\mathrm{SFG}}(\mathbf{r}, t)$.) Depending on the choice of excitation fields, it may be possible to explicitly detect the two individual $\mathbf{P}^{(2)}(\mathbf{k_s}, t)$ contributions; in time domain experiments, given well-separated time-ordered pulses, it is possible to detect only one of the two $\mathbf{k_s}$ SFG contributions. Conversely, in frequency domain experiments, time ordering of the applied fields is not possible; therefore, the individual $\mathbf{P}^{(2)}(\mathbf{k_s}, t)$ contributions will always be simultaneously detected.

In a similar manner, in formulating theoretical descriptions of the response function, $\mathbf{R}^{(2)}$, a given experiment may only be sensitive to a part of the response, and it is convenient to discard portions that do not contribute significantly.[61] This is accomplished by identifying terms in the response function that oscillate in time so as to phase cancel with those from the applied fields and by subsequently discarding the remaining terms. This is called the RWA. Computationally, this approximation allows for inclusion of only fully resonant Louiville space pathways and depends implicitly on the reference or model system being considered.[55,61,65] The RWA is a computational convenience; it is possible to include the entire response function and perform the integration in eq 3 (or presented specifically for second-order processes such as SFG in eq 5 below) explicitly.[67]

Note that a particular experiment measures either the modulus of the complex $\mathbf{P}^{(N)}(\mathbf{k_s}, t)$ (homodyne detection) or its' real or imaginary parts (heterodyne detection).[68,66] Methods using interference effects (via homodyne detection) between bulk and interfacial contributions to an SFG signal have also been used to separately measure the real and imaginary contributions at aqueous quartz interfaces.[16,69] The real and imaginary parts of the response contain information that is not obtainable via measuring the modulus of the signal.[3,16] This will be discussed further in section 8. We proceed by demonstrating how the limits of ideal frequency and impulsive fields simplify calculation of the polarization.

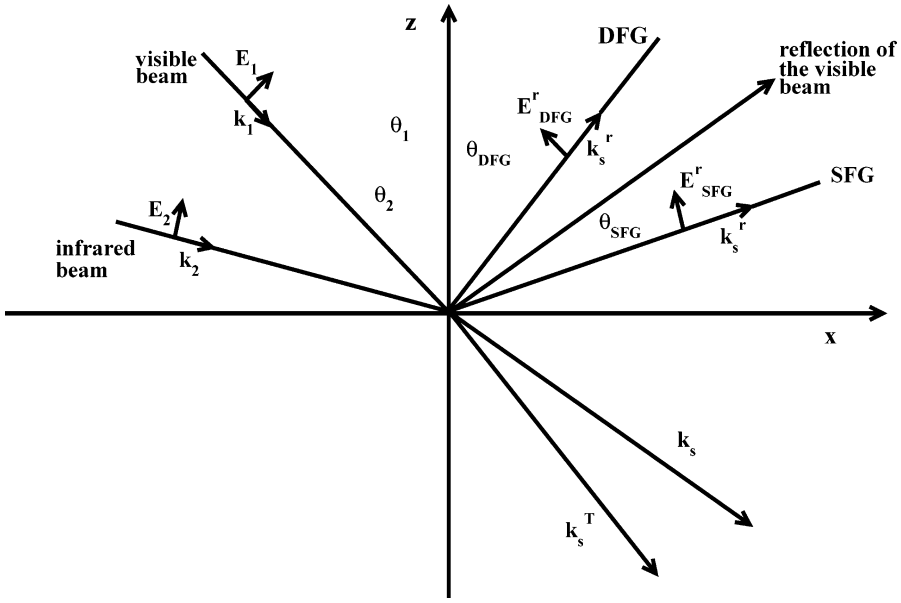

Figure 1. Coplanar geometry of the incident, reflected, and transmitted beams. θ_1 (θ_2) is the angle of incidence with respect to the *z*-axis of the visible (IR) field. θ_{SFG} (θ_{DFG}) is the angle at which the generated SFG (DFG) signal is radiated. $\mathbf{k}_1$ ($\mathbf{k}_2$) is the wave vector of the visible (IR) field. $\mathbf{k}_s^r$ ($\mathbf{k}_s^T$) is the wave vector of the reflected (transmitted) field, and $\mathbf{k}_s = \mathbf{k}_1 + \mathbf{k}_2$. All incident fields are assumed to lie in the same *xz* plane, which is normal to the surface.

3. Calculating the Polarization in Limiting Cases—Monochromatic and Impulsive Light

The second-order time-dependent polarization is defined by:[24,55,57,70,71]

$$\mathbf{P}^{(2)}(\mathbf{k}_s, t) = e^{i\mathbf{k}_s\cdot\mathbf{r}} \int_0^\infty d\tau_1 \int_0^\infty d\tau_2\, \mathbf{R}^{(2)}(\tau_1,\tau_2) : \mathbf{E}_1(t-\tau_1)\,\mathbf{E}_2(t-\tau_2) \quad (5)$$

In eq 5, $\mathbf{R}^{(2)}(\tau_1,\tau_2)$ is the system's second-order response function (a real quantity), τ_1 and τ_2 represent time delays between the first and the second fields and the second field and the time of signal detection, respectively. Note that the symbol ":" denotes contraction of the two-dimensional tensor (response or susceptibility) with the fields. A direct relationship between this quantity and the second-order frequency-dependent susceptibility can be established by representing the time-dependent components of the applied fields as their Fourier transform:

$$\mathbf{P}^{(2)}(\mathbf{k}_s, t) = \frac{e^{i\mathbf{k}_s\cdot\mathbf{r}}}{4\pi^2} \int_{-\infty}^\infty d\omega_1 \int_{-\infty}^\infty d\omega_2 \int_0^\infty d\tau_1 \int_0^\infty d\tau_2\, \mathbf{R}^{(2)}(\tau_1,\tau_2) : \mathbf{E}_1(\omega_1)\,\mathbf{E}_2(\omega_2)\, e^{-i\omega_1(t-\tau_1)-i\omega_2(t-\tau_2)} \quad (6)$$

The double Fourier−Laplace transform of the system's response function is now identified as the second-order susceptibility, χ:[55,70]

$$\chi^{(2)}(\omega_1,\omega_2) = \int_0^\infty d\tau_1 \int_0^\infty d\tau_2\, \mathbf{R}^{(2)}(\tau_1,\tau_2)\, e^{i\omega_1\tau_1} e^{i\omega_2\tau_2} \quad (7)$$

Because the susceptibility results from a Fourier−Laplace transform of the (real) response function, it is a complex quantity (the Fourier transform of the response function is, however, a real function). Substitution of eq 7 into eq 6 gives the time-dependent polarization in terms of the back Fourier transform of the product of the frequency domain fields and susceptibility:

$$\mathbf{P}^{(2)}(\mathbf{k}_s, t) = \frac{e^{i\mathbf{k}_s\cdot\mathbf{r}}}{(2\pi)^2} \int_{-\infty}^\infty d\omega_1 \int_{-\infty}^\infty d\omega_2\, \chi^{(2)}(\omega_1,\omega_2) : \mathbf{E}_1(\omega_1)\,\mathbf{E}_2(\omega_2)\, e^{-it(\omega_1+\omega_2)} \quad (8)$$

Fourier transforming the polarization with respect to time gives the frequency-dependent polarization where the signal frequency, Ω_s, is the transform variable conjugate to *t* and $\omega_s = \omega_1 + \omega_2$ (note that ω_s, the signal field, is distinct in our notation from ω_{SFG}, the particular case of a sum frequency signal):

$$\mathbf{P}^{(2)}(\mathbf{k}_s,\Omega_s) = \frac{e^{i\mathbf{k}_s\cdot\mathbf{r}}}{(2\pi)^2} \int_{-\infty}^\infty d\omega_1 \int_{-\infty}^\infty d\omega_2\, \chi^{(2)}(\omega_1,\omega_2) : \mathbf{E}_1(\omega_1)\,\mathbf{E}_2(\omega_2) \int_{-\infty}^\infty dt\, e^{-it(\omega_s-\Omega_s)} \quad (9)$$

$$\mathbf{P}^{(2)}(\mathbf{k}_s,\Omega_s) = \frac{e^{i\mathbf{k}_s\cdot\mathbf{r}}}{2\pi} \int_{-\infty}^\infty d\omega_1 \int_{-\infty}^\infty d\omega_2\, \delta(\omega_s-\Omega_s)\, \chi^{(2)}(\omega_1,\omega_2) : \mathbf{E}_1(\omega_1)\,\mathbf{E}_2(\omega_2) \quad (10)$$

Unlike eq 7, causality does not require a Fourier−Laplace transform because no system function is directly involved in the transform. Integration of the complex exponential over *t*, the time of signal detection, results in the δ function in eq 10. In the limit that the applied fields are monochromatic (the limit in which most frequency domain SFG experiments are performed), they may be represented as complex exponentials in the time domain and will be δ functions in the frequency domain: $\mathbf{E}(\omega_i) = 2\pi\,\mathbf{E}_i\,\delta(\omega_i - \Omega_i)$. Thus, an ideal frequency domain experiment directly probes the susceptibility:

$$\mathbf{P}^{(2)}(\mathbf{k}_s,\Omega_s) = 2\pi\, e^{i\mathbf{k}_s\cdot\mathbf{r}}\,\chi^{(2)}(\Omega_1,\Omega_2) : \mathbf{E}_1\mathbf{E}_2\,\delta(\omega_s - \Omega_s) \tag{11}$$

Note that as a result of the form of χ, $\Omega_s = \Omega_1 + \Omega_2$ is the signal frequency and is at the sum of the input frequencies; χ is described in section 7. In an SFG experiment, both frequencies would be positive, and a sum frequency would be detected. In a DFG experiment, one of the input frequencies would have a negative sign associated with it, and a difference frequency would be generated.

The limit of ideal frequency (monochromatic applied fields) is just one common means of simplifying the integrals necessary to calculate the second-order polarization. The opposite limit, the impulsive limit, occurs when the fastest material time scale is much longer than the durations of the applied fields. This limit is often assumed in theoretical developments for simplification purposes but generally is not truly justifiable—temporal pulse durations are not currently faster than even the shortest vibrational time scale.[55] In this limit, the applied field's temporal envelopes behave as δ functions, making the evaluation of eq 5 trivial. The resulting expression for an impulsive field at some time $\tilde{\tau}$ is

$$\mathbf{E}_i(\tau') = \mathbf{E}_i\,\delta(\tau' - \tilde{\tau})\, e^{-i\omega_i\tilde{\tau}} \tag{12}$$

$$\mathbf{P}^{(2)}(\mathbf{k}_s, t) = e^{i\mathbf{k}_s\cdot\mathbf{r}}\,\mathbf{R}^{(2)}(t - \tilde{\tau}_1, t - \tilde{\tau}_2) : \mathbf{E}_1\mathbf{E}_2\, e^{-i(\omega_1\tilde{\tau}_1 + \omega_2\tilde{\tau}_2)} \tag{13}$$

Note that the applied fields in eq 12 can also have an exponential phase factor associated with them.[72] While eq 12 implies that the experiment probes the entire response function, finite, yet short, pulses (that do not have the infinite frequency spectrum that a δ function pulse would contain) are only resonant with certain parts of the response function. To correct for this deficiency, it is useful to write the response function in terms of Louiville space pathways.[55] In this language, one should only include fully resonant Louiville space pathways of the susceptibility (response) tensor in the polarization calculation—this is equivalent to invoking the RWA.[55,65,73] In practice, this limit is commonly assumed for simplicity in calculating the polarization; it makes evaluation of the integrals in eq 5 trivial. In this case, it is *necessary* to *only* include pathways that are expected to contribute for a given set of fields and a relevant model system.[55,72]

4. Measured Intensity Including Dielectric Effects from the Interfacial Boundaries

Because interfaces necessarily include dielectric boundaries, the equations derived thus far need to be modified accordingly—the measured signal will include factors due to interactions with the boundaries.[74−76] The fields in the above derivations are local to the medium, and SFG excitation fields must travel through the vacuum before overlapping at the interface (for liquid/vapor or gas/solid interfaces) or through some other medium when considering a buried interface. When the fields combine at the interface, a second-order nonlinear signal is produced that interacts with the dielectric boundaries. Hence, the observed fields must be related to the laboratory-generated fields through Fresnel coefficients.[24,60,77] In a boundless medium, the Fresnel coefficients reduce to unity, and the laboratory and local fields are the same.[74]

Experimentally, it is the intensity generated at the sum frequency of the two input beams that is measured (in typical homodyne detection experiments). Equation 14[24,45,70,74,78] describes the relationship between the field, $\mathbf{E}(\mathbf{r},\omega_s)$, and the measured intensity, $\boldsymbol{I}(\omega_s)$, generated at the sum frequency of the two input fields:

$$\boldsymbol{I}(\omega_s) = \frac{c\sqrt{\epsilon_1(\omega_s)}|\mathbf{E}(\mathbf{r},\omega_s)|^2}{2\pi} \tag{14}$$

$\mathbf{E}(\mathbf{r},\omega_s)$ is found through the use of (nonlinear) Maxwell's wave equation—knowing the nonlinear polarization one can solve for the field.[24,79,80] The exact form of the relationship between the nonlinear polarization and the measured intensity generally depends on the boundary conditions of the medium, the direction that $\mathbf{E}(\mathbf{r},\omega_s)$ propagates in, how well phase matching can be achieved, whether the slowly varying envelope approximation is made, and the form of the applied fields, i.e, monochromatic, Gaussian, etc. In general, the local fields are approximated as monochromatic, and the slowly varying envelope approximation is assumed to be valid. Explicit expressions using various approximations are available in the literature.[24,45,60,74] Generally, the intensity is found to be proportional to the square of the sum frequency multiplied by the amplitude of the nonlinear polarization:

$$\boldsymbol{I}(\omega_s) \propto \omega_s^2\,|\,\mathbf{P}(\omega_s)\, e^{i\mathbf{k}_s\cdot\mathbf{r}}\,|^2 \tag{15}$$

The proportionality coefficients include the Fresnel factors that are typically calculated using an appropriate model of the experimental setup.[14] To directly compare theoretical and experimental spectra, it is necessary to include the Fresnel factors—especially when comparing relative intensities from different polarization conditions.[2,14] Note that experimental spectra are sometimes presented as the second-order susceptibility itself—correcting for factors such as the leading ω_s^2 dependence—or more often as simply the observed SFG intensity.

As demonstrated in section 3, in the limit of monochromatic fields, the polarization directly probes the susceptibility (eq 11). Following from eq 15, in this limit, the measured intensity will also directly probe the (the squared modulus of the) susceptibility tensor of the system. In total, the surface susceptibility tensor contains 27 elements. Consideration of symmetry conditions for a typical azimuthally isotropic interface requires all but seven elements of the susceptibility tensor to vanish because the elements need to be invariant with respect to symmetry operations that preserve the (azimuthal) symmetry.[63] Additionally, of the seven nonvanishing components, only four are, in general, unique ($\chi_{xzx} = \chi_{yzy}$, $\chi_{xxz} = \chi_{yyz}$, $\chi_{zxx} = \chi_{zyy}$, χ_{zzz}). Here, the subscripts on χ are the Cartesian directions in the laboratory frame.[78,81] By utilizing different polarization conditions, it is possible to directly probe three of the four nonvanishing susceptibility tensor components independently.[24,78,81,82] Note that for chiral surfaces different selection rules apply, and it is possible to probe different susceptibility tensor components.[24,59]

Each of the three light fields (with corresponding frequencies ω_{SFG}, ω_{vis}, and ω_{IR}) in SFG experiments can be either S or P polarized. S polarized light has a polarization vector parallel to the interface, and the P polarization is at an angle tilted to the surface and lies in a plane that is perpendicular to the interface. If the *xy* plane is taken to be the interface, it is usually defined that S polarized light has a single Cartesian polarization vector component along the *y*-axis $b\,\hat{\boldsymbol{y}}$ while P the vector lies in the *xz* plane with components $\hat{c}\boldsymbol{x}$

$+ \hat{dz}$.[77,78,83] Different combinations of S and P polarized fields allow for direct measurement of the following tensor elements:[78,81,84]

$$\chi^{(2)}_{\text{eff,SSP}} = \sin(\beta_{\text{IR}})\, L_{yy}(\omega_{\text{SFG}})\, L_{yy}(\omega_{\text{vis}})\, L_{zz}(\omega_{\text{IR}})\, \chi_{yyz} \quad (16)$$

$$\chi^{(2)}_{\text{eff,SPS}} = \sin(\beta_{\text{vis}})\, L_{yy}(\omega_{\text{SFG}})\, L_{zz}(\omega_{\text{vis}})\, L_{yy}(\omega_{\text{IR}})\, \chi_{yzy} \quad (17)$$

$$\chi^{(2)}_{\text{eff,PSS}} = \sin(\beta_{\text{SFG}})\, L_{zz}(\omega_{\text{SFG}})\, L_{yy}(\omega_{\text{vis}})\, L_{yy}(\omega_{\text{IR}})\, \chi_{zyy} \quad (18)$$

$$\begin{aligned}\chi^{(2)}_{\text{eff,PPP}} = &-\cos(\beta_{\text{SFG}})\cos(\beta_{\text{vis}})\sin(\beta_{\text{IR}})\, L_{xx}(\omega_{\text{SFG}})\\ &L_{xx}(\omega_{\text{vis}})\, L_{zz}(\omega_{\text{IR}})\, \chi_{xxz} - \cos(\beta_{\text{SFG}})\sin(\beta_{\text{vis}})\cos(\beta_{\text{IR}})\\ &L_{xx}(\omega_{\text{SFG}})\, L_{zz}(\omega_{\text{vis}})\, L_{xx}(\omega_{\text{IR}})\, \chi_{xzx} +\\ &\sin(\beta_{\text{SFG}})\cos(\beta_{\text{vis}})\cos(\beta_{\text{IR}})\, L_{zz}(\omega_{\text{SFG}})\, L_{xx}(\omega_{\text{vis}})\\ &L_{xx}(\omega_{\text{IR}})\, \chi_{zxx} + \sin(\beta_{\text{SFG}})\sin(\beta_{\text{vis}})\sin(\beta_{\text{IR}})\, L_{zz}(\omega_{\text{SFG}})\\ &L_{zz}(\omega_{\text{vis}})\, L_{zz}(\omega_{\text{IR}})\, \chi_{zzz}\end{aligned} \quad (19)$$

Here, L represents the Fresnel factors for the given fields (linear Fresnel factors for the visible and IR fields and a nonlinear factor for the sum frequency field),[22] and $\beta(\omega_i)$ is the angle that the field at frequency ω_i makes with respect to the surface normal. We use $\chi^{(2)}_{\text{eff}}$ to denote the effective susceptibility—unlike $\chi^{(2)}_{ijk}$, $\chi^{(2)}_{\text{eff}}$ explicitly accounts for the Fresnel factors. The S and P indices on $\chi^{(2)}_{\text{eff},\alpha\beta\gamma}$ denote how the fields ω_{SFG}, ω_{vis}, and ω_{IR}, respectively, are polarized, i.e., S or P. In the above expressions, because of the chosen experimental geometry, three of the polarization conditions (SSP, SPS, and PSS) directly probe single susceptibility tensor components while the PPP condition has components of all unique *allowed* Cartesian tensor elements.

5. Wave Vector and Phase Matching Considerations

In coherent nonlinear optical experiments, the signal is generated at a well-defined angle in the laboratory frame that is determined by the wave vector of the incident radiation. However, only certain experimental geometries will generate a desired $\mathbf{P}^{(N)}(\mathbf{k_s})$ signal. The required geometries must satisfy phase matching conditions that are a consequence of the input wave vector choice. To understand the phase matching conditions that need to be met, consider a monochromatic plane wave, $\exp(i\mathbf{k_j}\cdot\mathbf{r} - i\omega_j t)$, and its' associate wave vector, $\boldsymbol{k}_\mathbf{j}$. Its' frequency, ω_j, and wave vector are related by the complex refractive index, $n(\omega_j) = \text{Re}\{n(\omega_j)\} + i\,\text{Im}\{n(\omega_j)\}$:[57,62]

$$\mathbf{k_j} = \frac{n(\omega_j)\,\omega_j\,\mathbf{u_j}}{c} \quad (20)$$

Here, c is the speed of light, and $\mathbf{u_j}$ is a unit vector, which gives the direction of the wave vector. Each applied field then has an angle of incidence, θ_j, and a distinct time-dependent phase, ϕ_j, associated with it (see Figure 1):

$$\phi_j(t) = \frac{\text{Re}\{n(\omega_i)\}\,\omega_j}{c}\mathbf{u_j}\cdot\mathbf{r} - \omega_j t \quad (21)$$

In the context of second-order experiments, when the two incident wave vectors of the applied fields at an interface add, $\mathbf{k}_1 + \mathbf{k}_2$, an SFG/SHG signal is generated. Alternatively, when $\mathbf{k_s} = \pm(\mathbf{k}_1 - \mathbf{k}_2)$, a DFG signal is generated. Because the incident field's wave vectors are overlapped at the medium's interface, the field associated with $\mathbf{k_s}$ will be transmitted through the medium and also reflected from the surface of the medium (except for the case of total internal reflection). In the electric dipole approximation (in isotropic media), both the reflected and the transmitted signals are interface specific. If bulk quadrupolar contributions are important, the transmitted signal may contain a significant contribution from the bulk that is not always separable from the interfacial signature.[44,45,85] Snell's laws, in conjunction with medium specific properties and the incident field's wave vectors, must be considered when determining the wave vector of the reflected, $\mathbf{k_s^{(r)}}$, and transmitted, $\mathbf{k_s^{(T)}}$, signals.

It should be noted that although the two incident field's wave vectors initially may combine to give $\mathbf{k}_1 + \mathbf{k}_2$ and/or $\mathbf{k_s} = \pm(\mathbf{k}_1 - \mathbf{k}_2)$, it is not guaranteed that a measurable signal will be reflected. This is due to phase matching conditions, a consequence of energy and momentum conservation, that must be satisfied. This consideration leads to SFG and DFG signals only being detectable at angles that satisfy the following equations (in a typical SFG experimental geometry detailed in Figure 1):[62]

$$\sin(\theta_{\text{DFG}}) = \frac{\omega_1\sin(\theta_1) + \omega_2\sin(\theta_2)}{\omega_1 + \omega_2} \quad (22)$$

$$\sin(\theta_{\text{SFG}}) = \frac{\omega_1\sin(\theta_1) - \omega_2\sin(\theta_2)}{\omega_1 - \omega_2} \quad (23)$$

Note that although eq 22 always has a solution, eq 23 does not. Specifically, for the given conditions, this means that SFG will *always* emit a signal while DFG will only emit a signal when eq 24 is satisfied

$$\left[\frac{\omega_1\sin(\theta_1) - \omega_2\sin(\theta_2)}{\omega_1 - \omega_2}\right]^2 \le 1 \quad (24)$$

6. SFG Detection Techniques Including Those Beyond the Monochromatic Limit

6.1. Alternative Polarization Conditions: Polarization Mapping

Experimentally obtained SFG spectra heavily rely upon fitting techniques to deduce important spectral features even for relatively simple interfacial systems (see, e.g., section 8.2.1); spectra generally have convoluted peaks, and spectral fitting techniques serve to further separate and resolve these peaks. Fitting of spectra is generally performed via a mathematical/theoretical approach, but it was recently shown[82,86,87] that polarization mapping experiments can benefit the spectral fitting process. This method is highly effective when there is a high density of vibrational modes present at the interface in a particular spectral range, which makes resolution and identification of individual vibrational peaks difficult.

Polarization mapping,[88] also used in SHG applications,[87,89] is accomplished by measuring spectra using a wide continuous range of different polarization conditions on the input and/or output field(s). Intermediate polarization conditions refer to light with a polarization vector rotated somewhere between the S and the P polarization. This method is effective

because different polarization conditions probe different parts of the susceptibility tensor providing sensitivity to different molecular orientations and vibrations in distinct chemical environments. Therefore, measuring and comparing spectra under different polarization conditions (that can be thought of as linear combinations of the independent polarization conditions) of the input/output field(s) can reveal individual peaks that might otherwise appear convoluted.[86,87]

Chen et al.[86] recently performed both theoretical and experimental investigations using the polarization mapping techniques on centrosymmetric bulk systems that were azimuthally isotropic at the interface. As mentioned above, it is possible to perform polarization mapping by changing several different experimental parameters. In this study, the intermediate polarization conditions all had the visible beam at 45° from the S polarization, and the IR field was P polarized. To map the polarization, the SFG signals were detected at different polarizations, ranging from S to P, via measuring the spectra at different polarization angles with a polarizer placed in front of the detector. Once the spectra were collected, the SSP and PPP spectra were fitted using standard techniques. Using the fitting parameters from this process allows the SFG spectra at other various polarization angles to be calculated. The calculated spectra for other various polarization angles should adequately reproduce their experimental spectra if the fitting parameters deduced from the SSP and PPP polarization conditions are correct. As Chen et al. note, this is generally not the case for the initial SSP and PPP parameters deduced. They proceed by adjusting the fitting parameters and refitting the SSP and PPP spectra. This process is repeated until the calculated spectra for the intermediate polarization conditions closely match those obtained experimentally thus validating the spectral fit.

Using this method, Chen et al. were able to clearly show that different vibrational modes in the same spectral region reached their maximum intensity at distinct polarization angles and were, thus, able to perform improved spectral deconvolutions. To further test the method, an experimental model spectrum was constructed with overlapping vibrations. It was found that peak separation was even possible for two vibrational modes that had center frequencies only two wavenumbers apart (a 0.07% difference) and had little difference between their $\tau_{zzz/yyz} = \chi^{(2)}_{zzz}/\chi^{(2)}_{yyz}$ values. (In this case,[86] $\tau_{zzz/yyz}$ is the ratio between the PPP and the SSP susceptibility because the input and output fields were set to critical angles in a total internal reflection geometry, which effectively makes the Fresnel factors of the other possible contributing tensor elements zero.[90]) The polarization mapping method was also successfully applied by Chen et al. to deuterated polystyrene/air and histidine-tagged ubiquitin solution/deuterated polystyrene interfaces proving its value for interpreting spectra at complex interfaces.

6.2. Beyond the Monochromatic Limit

To date, most SFG experiments have been conducted and interpreted in the limit of monochromatic laser sources, thus directly probing the susceptibility via eq 11. However, taking advantage of the increasing availability of femtosecond pulsed lasers, it is possible to perform time domain (often referred to as FID, free induction decay) SFG experiments.[46−49] In contrast to the frequency domain, using short laser pulses does not imply the impulsive limit that would directly probe the response function in time because material response times are not all long as compared to the laser pulse durations. This implies, theoretically, that it is necessary to evaluate the time integration in eq 5 to calculate the nonlinear polarization. While this approach has not been adopted to date, using theoretical response functions calculated, e.g., via MD (see section 8), as inputs into eq 5 can aid in both design and interpretation of useful time domain experiments. Typically, this integration is avoided by still assuming the impulsive limit but only including fully resonant pathways of the response (susceptibility) tensor, i.e., making the RWA.[55] Alternatively, if a specific functional form can be associated with the response (susceptibility) tensor, then it may be possible to simply analytically integrate eq 5. However, in general, considering experiments outside of the monochromatic limit, it may be necessary to perform the numerical integrations explicitly.

6.2.1. Comparison of Time Domain and Frequency Domain Results

Comparison of Time Domain and Frequency Domain Results. An SFG experiment, under otherwise identical conditions, can be performed in either the time or the frequency domain from a theoretical standpoint; both measurements represent equivalent spectroscopic methods and can be simply related by Fourier transforming the polarization. For example, the time evolution of the polarization can be observed directly by using temporally short spectrally broad pulses. This can also be indirectly measured in frequency domain using temporally broad spectrally narrow pulses and Fourier transforming the resulting spectra to the time domain. Both of these techniques should, in principle, allow the vibrational dephasing time to be calculated.

Recently, it was shown,[46,48] while theoretically equivalent, that time and frequency domain measurements for a given IR-visible SFG experiment can be sensitive to different physical aspects of the system. This difference arises from the convolution of the resonant and nonresonant components of the system's susceptibility and how easily these experimentally measured components can be separated. Because the nonresonant susceptibility only contributes when the two fields overlap in time, as noted by Bonn et al.,[48] the resonant susceptibility, and hence the line shape, is more readily separable in time domain experiments, especially for time delays between the two incident fields, which are >500 fs. In a frequency domain experiment, time ordering of the pulses cannot be accomplished. Therefore, the resonant and nonresonant parts of the susceptibility will always be simultaneously present but can be separated by a variety of methods; note that the nonresonant contribution is typically constant (independent of frequency). Peak fitting is usually effective in separating these two components,[86] and isotopic dilution can also be performed.[19]

By performing both theoretical and experimental investigations,[46] Bonn et al. demonstrated that systems with homogeneous distributions of adsorption sites showed nominal difference between time and frequency determinations of line shape and vibrational dephasing times. Figure 2 details the same vibration (C−H stretch in acetonitrile) measured in both the frequency (top) and the time (bottom) regimes. The vibrational dephasing times were calculated from the time and frequency domain measurements and were 0.61 and 0.66 ps, respectively. Figure 3 shows the frequency (top) and time (bottom) domain measurements of the C−N stretch in acetonitrile. The calculated vibrational dephasing time

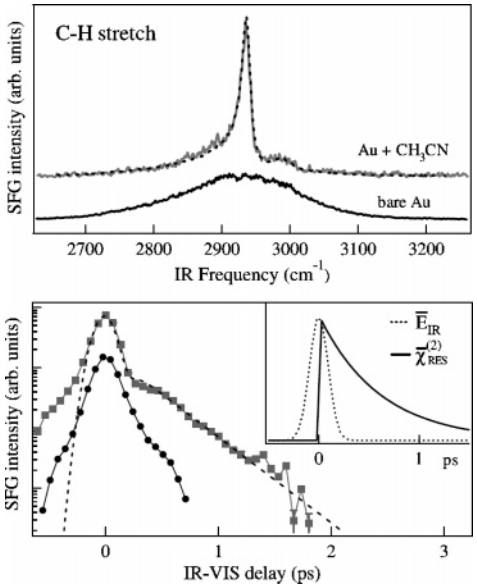

Figure 2. Frequency domain and time domain SFG measurements in the C−H stretch region of acetonitrile. Top: SFG spectra of a clean Au film (lower spectrum) and a Au film with acetonitrile. The weak feature around 3000 cm^{-1} corresponds to the asymmetric stretch vibration. Bottom: FID of clean Au film (offset) and a Au film with acetonitrile. The dashed lines in both panels are fits to the data with very similar vibrational dephasing times. The inset shows the IR field, $\bar{E}_{IR}$, and resonant susceptibility, $\bar{\chi}^{(2)}_{res}(t)$. Reprinted with permission from ref 48. Copyright 2003 Elsevier.

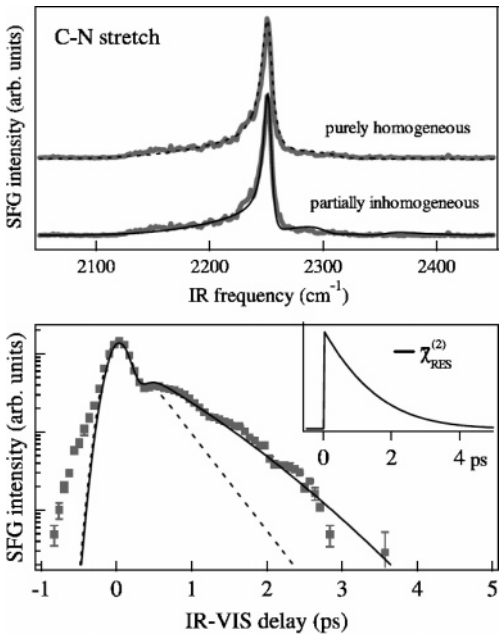

Figure 3. Frequency domain and time domain SFG measurements in the C−N stretch region of acetonitrile. Top: two (identical) SFG spectra of a Au film with acetonitrile. The upper (lower) spectrum is fitted assuming a homogeneous (inhomogeneous) distribution of adsorption sites. Bottom: FID of a Au film with acetonitrile. The data shown consist of an average of nine different data sets, of which the error bars show the spread. The dashed (solid) line is a calculation assuming a homogeneous (inhomogeneous) distribution of adsorption sites. The inset shows the resonant susceptibility, $\bar{\chi}^{(2)}_{res}(t)$, used for theoretical comparisons. Reprinted with permission from ref 48. Copyright 2003 Elsevier.

using the frequency domain data was 0.68 ps. As the dashed line in the lower panel of Figure 3 illustrates, a vibrational dephasing time of 0.68 ps does not correctly reproduce the time domain experiment. The pronounced difference in the time and frequency domain data was shown to be attributed to an inhomogeneous distribution of adsorption sites.[46,48] In this case, the time domain SFG experiments provided more accurate vibrational dephasing times and, thus, also more detailed spectral line shapes than frequency domain techniques—although it was only through the failure of the frequency domain data to accurately reproduce the time domain experiment that revealed the existence of an inhomogeneous distribution of adsorption sites. This investigation clearly demonstrates the utility and complimentary nature of using both time and frequency domain techniques.

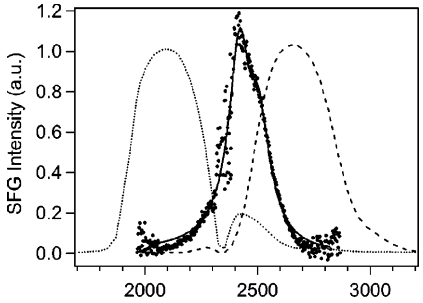

Figure 4. Frequency domain SFG spectrum of the $\nu_{(OD)}$ transition of D_2O at the CaF_2 interface (dotted line, experimental data; solid line, fit). IR pulse spectra used for the spectrally and time-resolved SFG measurements (STiR−SFG) are shown in thin dashed and dotted lines. Reprinted with permission from ref 47. Copyright 2005 American Institute of Physics.

6.2.2. Mixed Time Frequency Results

Recently, Benderskii et al.[47] developed a mixed time frequency domain technique, STiR−SFG (spectrally and time-resolved SFG), to measure SFG spectra, and, specifically, analyze the time evolution of interfacial hydrogen bonds in liquid D_2O systems by monitoring vibrational shifts in the OD stretch region; studies of this nature are critical because the time evolution of hydrogen bonds present at interfaces can profoundly affect the properties of water, and their characterization is, thus, necessary for a complete understanding of such systems. In this technique, traditional time domain techniques are used (employing spectrally broad temporally short pulses), but the SFG *signal* is dispersed through a monochromator such that it is the SFG *spectrum* that is recorded as a function of the delay time between the two applied fields. (In typical time domain measurements, it is the SFG intensity that is measured as a function of delay time between the two incident fields.) Specifically, a temporally short resonant IR pulse (≈70 fs) is applied to the interface of the system of interest, which creates a coherence and, hence, a first-order polarization. After a time delay, τ, a second temporally short off resonant visible pulse (≈40 fs) is applied. This pulse interacts with the coherence created by the IR pulse and probes the second-order polarization. In essence, this new technique uses a novel detection method to analyze information from experiments performed in the time domain.

The described mixed time frequency technique (STiR−SFG) was used by Benderskii et al. in a detailed study of a D_2O/CaF_2 (SSP geometry). As shown in Figure 4, the STiR−SFG spectrum was measured using IR pulses tuned to the blue and red sides of the OD stretch. Dynamics observed on both the blue and the red side of the OD stretch via the

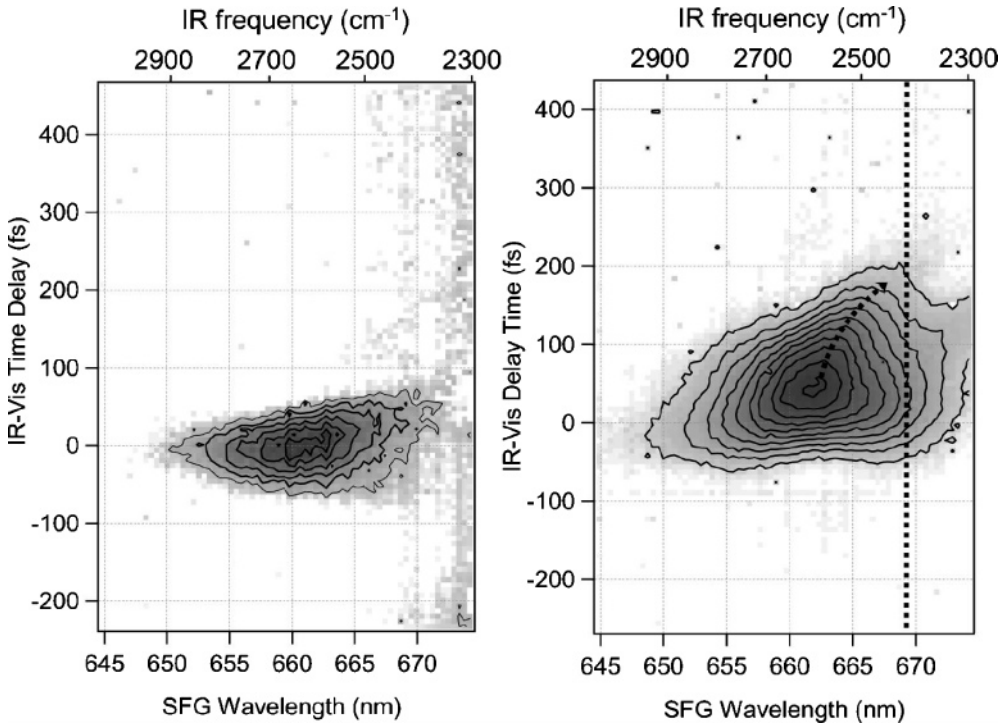

Figure 5. Right: STiR−SFG measurement of D_2O on the CaF_2 interface. IR excitation 2600 cm^{-1} (blue side). Left: instrument response function (IR-visible SFG−FROG cross-correlation). Vertical axis, IR-visible delay time (fs); horizontal axis, SFG wavelength; top, converted IR frequency. Reprinted with permission from ref 47. Copyright 2005 American Institute of Physics.

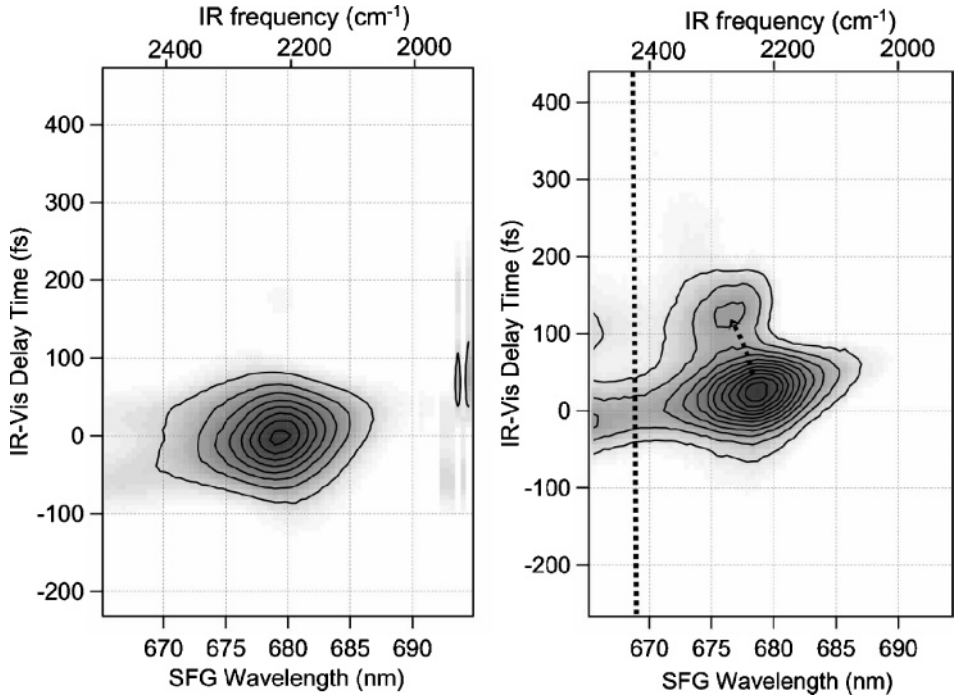

Figure 6. Right: STiR−SFG measurement of D_2O on the CaF_2 interface. IR excitation 2200 cm^{-1} (red side). Left: instrument response function (IR-visible SFG−FROG cross-correlation). Vertical axis, IR-visible delay time (fs); horizontal axis, SFG wavelength; top, converted IR frequency. Reprinted with permission from ref 47. Copyright 2005 American Institute of Physics.

STiR−SFG method are shown in Figures 5 and 6, respectively. After careful deconvolution of the instrument response function, measurements on the blue side showed a distinct red shift (≈60 cm^{-1}) to the OD stretch frequency on a time scale of ≈100−150 fs. Conversely, measurements on the red side of the OD stretch showed a distinct blue shift to the OD stretch frequency (≈50 cm^{-1}) in the first 130 fs and a pronounced recursion at 125 ± 10 fs. The differences in the spectra taken on the blue and red sides of the OD stretch highlight the heterogeneous nature of the hydrogen bond distribution in D_2O. Specifically, in conjunction with theoretical simulations, Benderskii et al. have been able to suggest that there is not uniformity in the strength of hydrogen bonds present in interfacial water, and rather, there exists distinct subensembles of relatively stronger (red side) and weaker (blue side) hydrogen bond structures.

7. Microscopic Expression for $\chi^{(2)}$

7.1. $\chi(\omega_1,\omega_2)$ in the Dipole Approximation

The systems susceptibility, χ, contains all of the information about the material system and is, thus, the focus of theoretical investigations into SFG interfacial vibrational spectroscopy. To calculate χ or, equivalently, the system response function, $\mathbf{R}^{(2)}$, it is necessary to develop a microscopic description of it. Furthermore, it is desirable to represent the response function in a form amenable to calculation and one that can exploit the power of MD interfacial simulations. MD is capable of accurately describing both the structure and the dynamics of even complex interfaces.[2−5,9−12,91−93] Specifically, it will be shown that the SFG response function is proportional to the imaginary part of the one time cross-correlation function of the system dipole and polarizability.[1−4,6]

To pursue this goal, starting from density matrix theory and using perturbative techniques, a formal expression for the second-order susceptibility in the dipole approximation can be derived.[4,24,57,94] Using this method, $\chi^{(2)\mathrm{SFG}}_{ijk}(\omega)$ is defined by a sum of six terms (shown below).[5,57] Four of the terms contribute to the resonant SFG signal (contained in R_1 and R_2), and the remaining contribute to the nonresonant portion of the signal (NR_1 and NR_2). The two terms in R_2 contain the expressions $(\omega_{\mathrm{IR}} + \omega_{ng} + i\gamma_{ng})$ and may initially appear to be nonresonant; γ is an arbitrary convergence parameter in time[95] that is frequently interpreted physically as a dipole dephasing rate[5,57] that would be responsible for a single mode's homogeneous line width in the frequency domain. Inclusion of these terms in the resonant susceptibility is, however, necessary to develop a general theory. Neglecting these contributions results in an expression only valid when $\hbar\omega \ll kT$, where k is Boltzmann's constant and T is the system temperature (this is equivalent to making the RWA in this case). Note that although we use ω_{IR} and ω_{vis}, this is easily generalizable to two arbitrary applied fields.

In the frequency domain, $\chi^{(2)\mathrm{SFG}}_{pqr}(\omega)$ takes the form:

$$\chi^{(2)\mathrm{SFG}}_{pqr}(\omega_{\mathrm{SFG}},\omega_{\mathrm{vis}},\omega_{\mathrm{IR}}) = \sum_{g,n,m} (\rho^{(0)}_g)\,(R_1 + R_2 + NR_1 + NR_2)$$

$$R_1 = \left[\frac{\mu^p_{gn}\,\mu^q_{nm}}{(\omega_{\mathrm{SFG}} - \omega_{ng} + i\gamma_{ng})} - \frac{\mu^q_{gn}\,\mu^p_{nm}}{(\omega_{\mathrm{vis}} + \omega_{ng} + i\gamma_{ng})}\right]\left[\frac{\mu^r_{mg}}{(\omega_{\mathrm{IR}} - \omega_{mg} + i\gamma_{mg})}\right]$$

$$R_2 = \left[\frac{\mu^q_{nm}\,\mu^p_{mg}}{(\omega_{\mathrm{SFG}} + \omega_{mg} + i\gamma_{mg})} - \frac{\mu^p_{nm}\,\mu^q_{mg}}{(\omega_{\mathrm{vis}} - \omega_{mg} + i\gamma_{mg})}\right]\left[\frac{\mu^r_{gn}}{(\omega_{\mathrm{IR}} + \omega_{ng} + i\gamma_{ng})}\right]$$

$$NR_1 = \frac{\mu^q_{gn}\,\mu^p_{mg}\,\mu^r_{nm}}{(\omega_{\mathrm{SFG}} + \omega_{mg} + i\gamma_{mg})\,(\omega_{\mathrm{vis}} + \omega_{ng} + i\gamma_{ng})}$$

$$NR_2 = \frac{\mu^p_{gn}\,\mu^q_{mg}\,\mu^r_{nm}}{(\omega_{\mathrm{SFG}} - \omega_{ng} + i\gamma_{ng})\,(\omega_{\mathrm{vis}} - \omega_{mg} + i\gamma_{mg})} \quad (25)$$

In the above expressions that define the six components of the second-order susceptibility, ω_{ng} is the frequency corresponding to the energy difference between energy levels n and g. In eq 25, $\rho^{(0)}_g$ is the initial state thermal population, and the sum is over vibronic levels. $\mu^{\eta}_{\alpha,\beta}$ is a dipole matrix element between states α and β for dipole vector component η in the laboratory frame.

Approximating $1/\omega_{\mathrm{SFG}} \approx 1/\omega_{\mathrm{vis}}$, the resonant contributions can be simplified by rewriting them in terms of polarizabilities and dipoles. Given the definition of polarizability (in the laboratory frame) in eq 26, the two resonant terms, R_1 and R_2, simplify to eqs 27 and 28, respectively.

$$\alpha_{pq}(\omega) = \sum_{g,n}\left[\frac{\mu^p_{gn}\,\mu^q_{ng}}{-\omega + \omega_{ng} - i\gamma_{ng}} + \frac{\mu^q_{gn}\,\mu^p_{ng}}{\omega + \omega_{ng} + i\gamma_{ng}}\right]\rho^{(0)}_g \quad (26)$$

$$R_1 = -\frac{\alpha^{pq}_{gm}\,\mu^r_{mg}}{(\omega_{\mathrm{IR}} - \omega_{mg} + i\gamma_{mg})} \quad (27)$$

$$R_2 = \frac{\mu^r_{gn}\,\alpha^{pq}_{ng}}{(\omega_{\mathrm{IR}} + \omega_{ng} + i\gamma_{ng})} \quad (28)$$

Let $\chi^{\mathrm{res}}_{pqr}$ denote only the sum of the resonant terms R_1 and R_2. Replacing the denominators in both of the resonant terms with the integral identities $\int_0^\infty \mathrm{d}t\, e^{-it(\omega-\omega_o-i\gamma)} = -i/(\omega - \omega_o - i\gamma)$ and $\int_0^\infty \mathrm{d}t\, e^{it(\omega+\omega_o+i\gamma)} = i/(\omega + \omega_o + i\gamma)$ and then taking the implied limit that γ goes to zero gives eq 29. Equation 30 follows as an exact rewrite of eq 29 and expresses the susceptibility in terms of the cross-correlation of the system dipole and polarizability.

$$\chi^{\mathrm{res}}_{pqr} = \left[\frac{i}{\hbar}\sum_{gm}\int_0^\infty e^{-i\omega_{mg}t}\,e^{i\omega_{\mathrm{IR}}t}\,\alpha^{pq}_{gm}\,\mu^r_{mg}\,\mathrm{d}t - \frac{i}{\hbar}\sum_{ng}\int_0^\infty e^{i\omega_{ng}t}\,e^{i\omega_{\mathrm{IR}}t}\,\alpha^{pq}_{ng}\,\mu^r_{gn}\,\mathrm{d}t\right]\rho^{(0)}_g \quad (29)$$

$$\chi^{\mathrm{res}}_{pqr} = \frac{i}{\hbar}\int_0^\infty \mathrm{d}t\, e^{it\omega_{\mathrm{IR}}}\langle\,\alpha_{pq}(t)\,\mu_r(0)\,\rangle - \frac{i}{\hbar}\int_0^\infty \mathrm{d}t\, e^{it\omega_{\mathrm{IR}}}\langle\,\mu_r(0)\,\alpha_{pq}(t)\,\rangle \quad (30)$$

In deriving eq 29 from 30, $\alpha_{pq}(t)$ is identified as the Heisenberg representation of the polarizability operator α at time t, and a sum over states is performed to remove a resolution of the identity.[96,97]

Expressing the correlation function in eq 30 explicitly as the sum of its' real and imaginary components reduces eq 30 to eq 31, below. Note that $\langle\,\mu_r(0)\,\alpha_{pq}(t)\,\rangle = C_{\mathrm{R}}(t) + iC_{\mathrm{I}}(t) = (\langle\,\alpha_{pq}(t)\,\mu_r(0)\,\rangle)^*$, and the subscripts R and I will be used throughout the article to represent the real and imaginary parts (both of which are themselves real) of complex quantities.[96] In the frequency domain, the time correlation function (TCF) is real and takes the form $C(w) = C_{\mathrm{R}}(\omega) +$

$C_I(\omega)$, where C_R is even ($C_R(\omega) = C_R(-\omega)$) while $C_I(\omega)$ is odd ($-C_I(\omega) = C_I(-\omega)$):[96,98,99]

$$\chi^{res}_{pqr}(\omega_{IR}) = \frac{2}{\hbar}\int_0^\infty dt\, e^{it\omega_{IR}}\, C_I(t) \tag{31}$$

Note that χ^{res}_{pqr} is presented as an explicit function of the IR frequency because the other optical frequencies are absorbed implicitly into the polarizability. Equation 31 is a nearly exact rewrite (exact other than substituting $1/\omega_{SFG} \approx 1/\omega_{vis}$) of the perturbation expression and is the central result of this section; it links the susceptibility to a TCF of the system's dipole and polarizability. The quantum mechanical TCF is amenable to calculation using classical MD supplemented by a suitable spectroscopic model via quantum correcting of the classical TCF;[3,100,101] while eq 31 includes the imaginary part of the TCF, classical TCF methods can only approximate the real part, but as will be detailed below, the real and imaginary parts of the TCF are simply related in the frequency domain.[102,103] Equation 31 is also a starting point for possible calculation of the quantum TCF using reduced dimensional models[71,104] or quantum dynamical approaches.[105,106]

The literature contains examples of using an expression similar to eq 31 but written in the RWA.[4,11,13] It will now be demonstrated that only in the high-frequency limit and because of the exact frequency relationship between the real and the imaginary components of the correlation function can R_2 be excluded from the resonant component of the susceptibility. In this approximation, the resonant susceptibility is given by only the first term in eq 29; that is, the resonant susceptibility is then given as the Fourier transform of the full TCF:

$$\chi^{res}_{pqr} = \frac{i}{\hbar}\sum_{gm}\int_0^\infty e^{-i\omega_{mg}t}\, e^{i\omega_{IR}t}\, \alpha^{pq}_{gm}\, \mu^{r}_{mg}\, dt = \frac{i}{\hbar}\int_0^\infty dt\, e^{i\omega_{IR}}\, \langle\, \alpha_{pq}(t)\, \mu_r(0)\,\rangle \tag{32}$$

To proceed, the correlation function is expressed as its' real and imaginary time-dependent components. Next, both the real and the imaginary components of the correlation function are represented as their corresponding Fourier transforms, and the order of integration is switched as follows:

$$\chi^{res}_{pqr} = \frac{i}{\hbar}\int_0^\infty dt\, e^{i\omega_{IR}t}\, [C_R(t) - iC_I(t)] \tag{33}$$

$$\chi^{res}_{pqr} = \frac{i}{2\pi\hbar}\int_0^\infty dt\, e^{i\omega_{IR}t}\int_{-\infty}^{\infty} d\omega\, e^{i\omega t}\, C_R(\omega) + \frac{1}{2\pi\hbar}\int_0^\infty dt\, e^{i\omega_{IR}t}\,(-i)\int_{-\infty}^{\infty} d\omega\, e^{i\omega t}\, C_I(\omega) \tag{34}$$

$$\chi^{res}_{pqr} = \frac{i}{2\pi\hbar}\int_{-\infty}^{\infty} d\omega\, C_R(\omega)\int_0^\infty dt\, e^{it(\omega_{IR}+\omega)} - \frac{i}{2\pi\hbar}\int_{-\infty}^{\infty} d\omega\, C_I(\omega)\int_0^\infty dt\, e^{it(\omega_{IR}+\omega)} \tag{35}$$

The integration over dt in eq 35 can easily be performed and results in a δ function and principle part contribution:[95]

$$\chi^{res}_{pqr} = \frac{i}{2\hbar}\, C_R(\omega_{IR}) + \frac{i}{2\hbar}\, C_I(\omega_{IR}) + \frac{P}{2\pi\hbar}\int_{-\infty}^{\infty} d\omega\, \frac{C_I(\omega) + C_R(\omega)}{\omega_{IR} + \omega} \tag{36}$$

Equation 36 contains the Fourier transform of both the real and the imaginary parts of the TCF in contrast to the exact result; eq 31 (after performing the time integration) is proportional to only the sum of the Fourier transform of the imaginary part of the TCF plus a principle part contribution. However, because there exists an exact detailed balance relationship between the real components of the frequency domain correlation function, $C_I(\omega) = \tanh(\beta\hbar\omega/2)\, C_R(\omega)$, eq 36 can be rewritten as:

$$\chi^{res}_{pqr} = \frac{i}{2\hbar}\,[1 + \coth(\beta\hbar\omega_{IR})]\, C_I(\omega_{IR}) + \frac{P}{2\pi\hbar}\int_{-\infty}^{\infty} d\omega\, \frac{C_I(\omega) + \coth(\beta\hbar\omega/2)\, C_I(\omega)}{\omega_{IR} + \omega} \tag{37}$$

In the high-frequency limit, where $\coth(\beta\hbar\omega/2) \rightarrow 1$, eq 37 is the correct expression relating the resonant susceptibility to the imaginary component of the correlation function.

Equation 32 has been used in the literature to calculate the resonant susceptibility, and in those cases, the full quantum TCF is approximated as the classical TCF.[5,4,11] Equation 32 is accurate at sufficiently high frequency, but when adopting a classical approach, it is better to link the classical correlation function to the quantum TCF via quantum correction approaches,[2,3,107] although quantum correction affects the magnitude of the signal more than the line shape. Furthermore, eq 32 is not accurate at lower frequencies where many interesting interfacial phenomena occur.[108,109] However, to date, SFG experiments have focused on high-frequency intramolecular vibrations due to technical limitations—most tunable IR lasers are not yet capable of probing lower frequencies. Even though some nonlinear crystals (e.g., GaSe) can generate IR beams with strong enough intensity in the lower wavenumbers, they are not widely applied. Current typical SFG experiments employ optical parametric amplifier-generated tunable IR radiation that have insufficient power to create measurable SFG signals below about 1000 cm^{-1}.[17,52,110] There are, however, free electron laser sources that produce sufficiently intense light for SFG experiments into the far IR.[108,109] Computationally, these regions of lower frequency can be analyzed[2,3] and have revealed novel low-frequency species present at the water/vapor interface.[2,3,7] These results will be discussed in section 8.

7.2. Quadrupole Contributions to $\chi^{(2)}$ from the Bulk

In three-wave mixing experiments where the dipole approximation is valid, $\chi^{(2)}$ vanishes for isotropic

media.[24,44,57,70,111,112] This property is what makes SFG a useful method for probing interfacial dynamics. When it is necessary to include higher order terms (i.e., quadrupole contributions) to the perturbed Hamiltonian, $\chi^{(2)}$ does not vanish for isotropic media.[44,70,111,113] Under these conditions, SFG probes not only the interface but also quadrupole contributions from the bulk.[44,85,13] (Bulk contribution in isotropic media via quadrupole interactions was first observed by Terhune and co-workers.[114]) There is no universal set of criteria for determining when quadrupole interactions will significantly contribute to the polarization, and the magnitude of their contribution must be considered on a case by case basis.[44]

Quadrupole contributions can be understood by considering the perturbed Hamiltonian, H', that includes both dipole and quadrupole contributions, respectively:

$$H'(t) = -\sum_i \mu_i E_i(t) - \sum_{i,j} q_{ij} \frac{\partial E_i(t)}{\partial r_j} \qquad (38)$$

In eq 38, r_j represents a system coordinate, and q_{ij} is the system's quadrupole moment. Starting from density matrix theory and using perturbative techniques, the susceptibility including dipole and quadrupole contributions can be derived.[13,44,45] The microscopic quadrupolar susceptibility is a fourth-ranked tensor and is the sum of three components: $\chi_{ijkl}^{(2)Q_s}$, $\chi_{ijkl}^{(2)Q_{IR}}$, and $\chi_{ijkl}^{(2)Q_{vis}}$. $\chi_{ijkl}^{(2)Q_s}$, defined in eq 39, contributes to the quadrupole polarization. It is generated by a dipolar coupling to the first two applied fields, ω_{IR} and ω_{vis}, and a quadrupolar coupling to the sum frequency field, $\omega_s = \omega_{IR} + \omega_{vis}$.[44] $\chi_{ijkl}^{(2)Q_{IR}}$ contributes to the dipolar polarization via dipolar coupling to E_{vis} and E_s and a quadrupolar coupling to ω_{IR}. $\chi_{ijkl}^{(2)Q_{vis}}$ contributes to the dipolar polarization via dipolar coupling to ω_{IR} and θ_s and a quadrupolar coupling to ω_{vis}. Theoretically, it is possible to separate dipole and quadrupole contributions to the polarization, but experimentally, it is *not* possible to fully separate *all* of the bulk's (quadrupole) contributions.[13,44,50,115] This is due to the nonunique definition of what defines the surface and bulk portions of the material. We proceed by deriving the resonant portion of the quadrupolar susceptibility in terms of TCFs starting from perturbative density matrix expressions.[13] The $\sum_{molecules}$ in the subsequent quadrupolar perturbative susceptibility terms is a sum over all molecules in the system. This summation arises because the perturbation expressions are based on the Hamiltonian of a single particle. As Morita notes, the summation on molecules must take into account local fields.[13] In analogy with presenting the interfacial dipolar contributions in TCF form, writing the quadrupolar contributions in terms of TCFs allows the use of classical MD techniques to calculate these contributions from molecularly detailed simulations. To date, no such calculation has been done. The explicit derivation is presented next for $\chi_{ijkl}^{(2)Q_s}$, and only the final result is shown for the other contributions. Perturbation theory gives $\chi_{ijkl}^{(2)Q_s}$ as:

$$\chi_{ijkl}^{Q_s} = \frac{1}{\hbar^2} \sum_{\text{molecules}} \sum_{mno} \rho_{oo}^{(o)} \left(\frac{q_{on}^{ij} \mu_{nm}^{k} \mu_{mo}^{l}}{(\omega_{no} - \omega_{SFG} - i\gamma_{no})(\omega_{mo} - \omega_{IR} - i\gamma_{mo})} + \frac{q_{on}^{ij} \mu_{nm}^{l} \mu_{mo}^{k}}{(\omega_{no} - \omega_{SFG} - i\gamma_{no})(\omega_{mo} - \omega_{vis} - i\gamma_{mo})} + \frac{q_{nm}^{ij} \mu_{on}^{k} \mu_{mo}^{l}}{(\omega_{nm} + \omega_{SFG} + i\gamma_{nm})(\omega_{mo} - \omega_{IR} - i\gamma_{mo})} + \frac{q_{nm}^{ij} \mu_{on}^{l} \mu_{mo}^{k}}{(\omega_{nm} + \omega_{SFG} + i\gamma_{nm})(\omega_{mo} - \omega_{vis} - i\gamma_{mo})} + \frac{q_{nm}^{ij} \mu_{on}^{l} \mu_{mo}^{k}}{(\omega_{mn} - \omega_{SFG} - i\gamma_{mn})(\omega_{no} + \omega_{IR} + i\gamma_{no})} + \frac{q_{nm}^{ij} \mu_{on}^{k} \mu_{mo}^{l}}{(\omega_{mn} - \omega_{SFG} - i\gamma_{mn})(\omega_{no} + \omega_{vis} + i\gamma_{no})} + \frac{q_{mo}^{ij} \mu_{on}^{l} \mu_{nm}^{k}}{(\omega_{mo} + \omega_{SFG} + i\gamma_{mo})(\omega_{no} + \omega_{IR} + i\gamma_{no})} + \frac{q_{mo}^{ij} \mu_{on}^{k} \mu_{nm}^{l}}{(\omega_{mo} + \omega_{SFG} + i\gamma_{mo})(\omega_{no} + \omega_{vis} + i\gamma_{no})} \right) \qquad (39)$$

Equation 39 possesses intrinsic permutation symmetry with respect to the IR and visible fields. In an analogous method to the derivation above for the susceptibility in the dipole approximation, the third and sixth terms and the fourth and fifth terms can be combined to reduce $\chi_{ijkl}^{(2)Q_s}$ to the six terms in eq 40:

$$\begin{aligned}
\text{terms 3 and 6} &= \frac{\mu_{on}^{k} q_{nm}^{ij} \mu_{mo}^{l}}{-\omega_{SFG} + \omega_{mn} - i\gamma_{mn}} \left(\frac{1}{\omega_{vis} + \omega_{no} + i\gamma_{no}} + \frac{1}{\omega_{IR} - \omega_{mo} + i\gamma_{mo}} \right) \\
&= \frac{-\mu_{on}^{k} q_{nm}^{ij} \mu_{mo}^{l}}{(\omega_{vis} + \omega_{no} + i\gamma_{no})(\omega_{IR} - \omega_{mo} + i\gamma_{mo})} \left(\frac{\omega_{SFG} + \omega_{nm} + i(\gamma_{no} + \gamma_{mo})}{\omega_{SFG} + \omega_{nm} + i\gamma_{mo}} \right) \\
&\approx \frac{-\mu_{on}^{k} q_{nm}^{ij} \mu_{mo}^{l}}{(\omega_{vis} + \omega_{no} + i\gamma_{no})(\omega_{IR} - \omega_{mo} + i\gamma_{mo})} \\
\text{terms 4 and 5} &= \frac{\mu_{on}^{l} q_{nm}^{ij} \mu_{mo}^{k}}{-\omega_{SFG} + \omega_{mn} - i\gamma_{mn}} \left(\frac{1}{\omega_{IR} + \omega_{no} + i\gamma_{no}} + \frac{1}{\omega_{vis} - \omega_{mo} + i\gamma_{mo}} \right) \\
&= \frac{-\mu_{on}^{l} q_{nm}^{ij} \mu_{mo}^{k}}{(\omega_{vis} - \omega_{mo} + i\gamma_{mo})(\omega_{IR} + \omega_{no} + i\gamma_{no})} \left(\frac{\omega_{SFG} + \omega_{nm} + i(\gamma_{no} + \gamma_{mo})}{\omega_{SFG} + \omega_{nm} + i\gamma_{nm}} \right) \\
&\approx \frac{-\mu_{on}^{l} q_{nm}^{ij} \mu_{mo}^{k}}{(\omega_{vis} - \omega_{mo} + i\gamma_{mo})(\omega_{IR} + \omega_{no} + i\gamma_{no})}
\end{aligned}$$

$$\chi_{ijkl}^{Q_s} = \frac{1}{\hbar^2}\sum_{\text{molecules}}\sum_{mno}\rho_{oo}^{(o)} \frac{q_{on}^{ij}\,\mu_{nm}^{k}\,\mu_{mo}^{l}}{(\omega_{no}-\omega_{\text{SFG}}-i\gamma_{no})\,(\omega_{mo}-\omega_{\text{IR}}-i\gamma_{mo})} + \frac{q_{on}^{ij}\,\mu_{nm}^{l}\,\mu_{mo}^{k}}{(\omega_{no}-\omega_{\text{SFG}}-i\gamma_{no})\,(\omega_{mo}-\omega_{\text{vis}}-i\gamma_{mo})} + \frac{-\mu_{on}^{l}\,q_{nm}^{ij}\,\mu_{mo}^{k}}{(\omega_{\text{vis}}-\omega_{mo}+i\gamma_{mo})\,(\omega_{\text{IR}}+\omega_{no}+i\gamma_{no})} + \frac{-\mu_{on}^{k}\,q_{nm}^{ij}\,\mu_{mo}^{l}}{(\omega_{\text{vis}}+\omega_{no}+i\gamma_{no})\,(\omega_{\text{IR}}-\omega_{mo}+i\gamma_{mo})} + \frac{q_{mo}^{ij}\,\mu_{on}^{l}\,\mu_{nm}^{k}}{(\omega_{mo}+\omega_{\text{SFG}}+i\gamma_{mo})\,(\omega_{no}+\omega_{\text{IR}}+i\gamma_{no})} + \frac{q_{mo}^{ij}\,\mu_{on}^{k}\,\mu_{nm}^{l}}{(\omega_{mo}+\omega_{\text{SFG}}+i\gamma_{mo})\,(\omega_{no}+\omega_{\text{vis}}+i\gamma_{no})} \quad (40)$$

In eq 40, only the terms that contain ω_{IR} can become appreciably resonant since the visible beam is tuned far from resonance. Again, we approximate $1/\omega_{\text{vis}} \approx 1/\omega_{\text{SFG}}$. This approximation allows us to write the *resonant* portion of $\chi_{ijkl}^{(2)Q_s}$ in terms of the quadrupole polarizability, β^{ijk}:

$$\beta^{ijk} = \frac{1}{\hbar}\sum_{on}\rho_{oo}^{(o)}\left(\frac{q_{on}^{ij}\,\mu_{no}^{k}}{\omega_{no}-\omega-i\gamma_{no}} + \frac{\mu_{on}^{k}\,q_{no}^{ij}}{\omega_{no}+\omega+i\gamma_{no}}\right) \quad (41)$$

$$\chi_{ijkl}^{(2)Q_s,\text{res}} = \frac{1}{\hbar}\sum_{\text{molecules}}\sum_{mo}\rho_{oo}^{(o)}\left(\frac{-\mu_{mo}^{l}\,\beta_{om}^{ijk}}{\omega_{\text{IR}}-\omega_{mo}+i\gamma_{mo}} + \frac{\beta_{mo}^{ijk}\,\mu_{om}^{l}}{\omega_{\text{IR}}+\omega_{mo}+i\gamma_{mo}}\right) \quad (42)$$

In eq 42, $\beta_{\delta,\epsilon}^{ijk}$ is the matrix element of the quadrupolar polarizability. An exact rewrite of eq 42 is possible using the same integral identities used in section 7.1. Note that this derivation closely follows that due to Morita[13] but does not invoke the RWA in analogy with the derivations in section 7.1. $\chi_{ijkl}^{(2)Q_s,\text{res}}$ now takes the form of a TCF suitable for molecular simulation:

$$\chi_{ijkl}^{(2)Q_s,\text{res}} = \frac{i}{\hbar}\sum_{\text{molecules}}\left[\int_0^\infty \mathrm{d}t\, e^{i\omega_{\text{IR}}t}\langle\,\beta^{ijk}(t)\,\mu^{l}(0)\,\rangle - \int_0^\infty \mathrm{d}t\, e^{i\omega_{\text{IR}}t}\langle\,\mu^{l}(0)\,\beta^{ijk}(t)\,\rangle\right] \quad (43)$$

In analogy, the resonant part of $\chi_{ijkl}^{(2)Q_{\text{IR}}}$ and $\chi_{ijkl}^{(2)Q_{\text{vis}}}$ may be written as follows:

$$\chi_{ijkl}^{(2)Q_{\text{IR}},\text{res}} = \frac{i}{\hbar}\sum_{\text{molecules}}\left[\int_0^\infty \mathrm{d}t\, e^{i\omega_{\text{IR}}t}\langle\,\alpha^{ij}(t)\,q^{kl}(0)\,\rangle - \int_0^\infty \mathrm{d}t\, e^{i\omega_{\text{IR}}t}\langle\,q^{kl}(0)\,\alpha^{ij}(t)\,\rangle\right] \quad (44)$$

$$\chi_{ijkl}^{(2)Q_{\text{vis}},\text{res}} = \frac{i}{\hbar}\sum_{\text{molecules}}\left[\int_0^\infty \mathrm{d}t\, e^{i\omega_{\text{IR}}t}\langle\,\beta^{kli}(t)\,\mu^{j}(0)\,\rangle - \int_0^\infty \mathrm{d}t\, e^{i\omega_{\text{IR}}t}\langle\,\mu^{j}(0)\,\beta^{kli}(t)\,\rangle\right] \quad (45)$$

The TCFs in eqs 43−45 can be expanded into their real and imaginary components. In each of the three equations, direct expansion into their respected correlation function's real and imaginary parts simply equates the resonant susceptibility to the integral over the imaginary component (which is real) of the correlation function. This expansion, and subsequent simplification, is in exact analogy to the (previously shown) steps required to transform eq 30 to eq 31 for the susceptibility in the dipole approximation.

7.3. Third-Order Contributions to the Sum Frequency Response: Charged Surfaces in Centrosymmetric Media

When properly designed, three-wave mixing experiments can probe both the second-order, $\chi^{(2)}$, and the third-order, $\chi^{(3)}$, susceptibilities. Techniques of this nature have been utilized in interfacial studies of solids since the 1960s,[116,117] but it has not been until more recently that liquid interfaces have been analyzed.[23,33,118,119] In the context of liquid interfaces, this method, sometimes referred to as electric field-induced SHG/SFG/DFG, relies on the presence of a charged species, such as surfactants,[119] which can create a static field, $\mathbf{E}_{\text{static}}$, that lies in the region of the interface and is local to the medium.[120] In this case, the observed polarization, in the limit of monochromatic fields, is given by:[23,120]

$$\mathbf{P} = \mathbf{P}^{(2)} + \mathbf{P}^{(3)} = \chi^{(2)} : \mathbf{E}_{\text{vis}}\,\mathbf{E}_{\text{IR}} + \chi^{(3)} \vdots \mathbf{E}_{\text{vis}}\,\mathbf{E}_{\text{IR}}\,\mathbf{E}_{\text{static}} \quad (46)$$

There are two main contributions to the third-order susceptibility. (i) The presence of three fields (two incident + static) gives rise to a third-order electronic nonlinear polarizability from the solvent. (ii) The symmetry is broken by the presence of $\mathbf{E}_{\text{static}}$; thus, it further extends the anisotropic interfacial region into normally centrosymmetric regions of the bulk.[23,120] Hence, contributions of $\chi^{(3)}$ to the observed polarization are inherently bulk in origin.[120] Furthermore, because the presence of the static field extends the interfacial region as described in (ii), the second-order susceptiblity will be more intense when charged species are present at the interface.[118,121]

The value of theoretical and experimental electric field-induced three-wave mixing investigations lies in their ability to deduce the electrostatic potential created by the charged species near the interfacial surface and monitor how the electrostatic potential inherently changes the nature of the interface. Because many interfaces—such as air/water and oil/water—are generally not exclusively present in a natural environment, such studies can provide highly relevant information for many environmentally important systems.

8. Applications of Theoretical SFG Spectroscopy to Aqueous Interfaces

Theoretical modeling of SFG vibrational spectroscopy using MD-based methods is a relatively young field with only a few existing studies, all but two of which consider

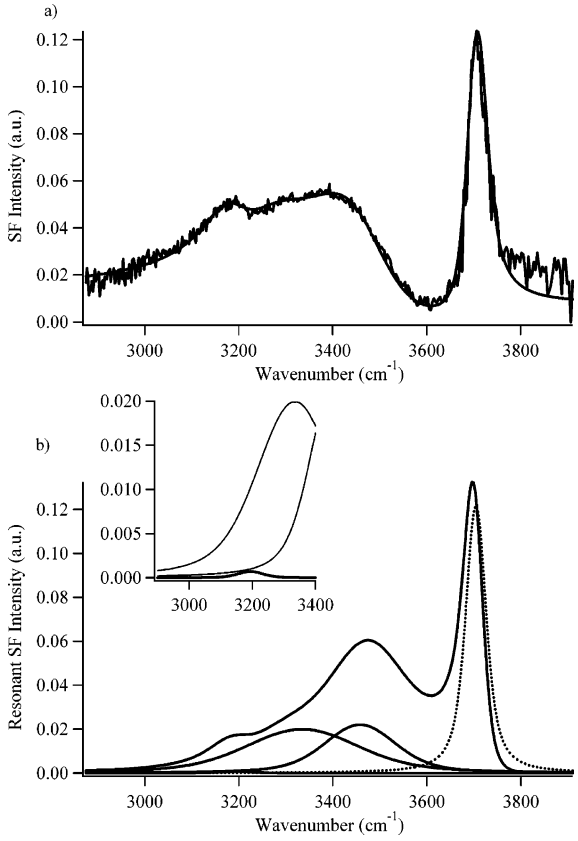

Figure 7. (a) SFG spectrum of the water/vapor interface taken under SSP polarization conditions. The smooth line is the best fit to the data. (b) Resonant SF response from the water/vapor interface. Also shown are the contributions from the different molecular species. The inset shows the 3200 cm^{-1} peak more clearly. Reprinted with permission from ref 134. Copyright 2004 American Chemical Society.

aqueous interfaces.[1−7,9,11−15,69,122] However, such studies clearly show great promise and are growing in importance due to their ability to provide a molecularly detailed description of interfacial species and their vibrations. These early studies have also demonstrated the ability to link a particular spectroscopic SFG signature to an interfacial vibrational mode—the principle goal of vibrational spectroscopy. Theoretical SFG spectra have also been used to identify multiple species in complex line shapes[3] and reveal lower frequency species that were previously undetected;[2,3] while experimental studies also have these abilities, in principle, they have been limited by technological barriers, such as difficulty in separately measuring the real and imaginary portions of the SFG signal[16] and the lack of intense tunable IR radiation sources.[17,108,109]

The use of MD-based methods to describe condensed phase (intramolecular) vibrational spectroscopy is widespread and highly effective.[67,101,123−133] The utility of theoretical input, in the case of SFG spectroscopy, can be even greater given the complex line shapes that are characteristic of interfaces. For example, Figure 7a shows the SSP SFG intensity for the O−H stretching region of the water/vapor interface obtained experimentally along with a deconvolution of the resonant part into possible component species (Figure 7b).[19,134] Clearly, the line shape is far more complex than the corresponding bulk line shape, which is nearly symmetric.[3,135,136]

Theoretical studies have also explicitly demonstrated the degree to which SFG spectroscopy is interface specific,[5] something that is difficult to ascertain experimentally. This kind of insight is particularly important at highly ordered aqueous interfaces, e.g., those on charged solids or when surfactants are present at interfaces. In such cases, third-order polarization contributions can be important because the (relatively) static electric field at the interface combines with the IR and visible fields to give a contribution at the sum frequency.[22] Simulations also have the ability to include other possible contributing phenomena like bulk quadrupolar contributions[13,16,44,45] or bulk contributions from noncentrosymmetric solids.[24] This can help disentangle the relative contributions in a straightforward manner, which is difficult to do so experimentally.[44] These issues will be considered separately below.

The first attempt at approximately modeling SFG spectroscopy considered the IR spectrum of the water/vapor interface[9] that had been reported experimentally a short time earlier.[25] For a bulk system, IR spectroscopy is typically calculated using linear response theory via the dipole−dipole autocorrelation function.[96,97,101] However, this spectrum is not sensitive to the interface due to the much smaller number of oscillators resident there as compared to the bulk. To obtain some surface selectivity, the study calculated the dipole correlation function for only molecules within a small distance of the Gibbs dividing surface; while this does not directly represent any physically measurable quantity, it is a reasonable approach to probe the interfacial vibrations. This study revealed the presence of free O−H oscillators at the interface and at the correct frequency. The study also demonstrated that adding methanol quenches the free O−H peak—in agreement with another early SFG experiment.[29] A similar approach was recently adopted by Mundy et al. in an ambitious ab initio MD simulation of the water/vapor interface that also identified the free O−H moiety and described the dipolar change as the water/vapor interface was approached.[7] This study also described the nature of the bonding at the water/vapor interface.

The first attempts to directly calculate an SFG signal did not consider liquid interfaces but rather the SFG spectrum of adsorbates at solid interfaces.[6,15] The authors first used a frequency domain approach.[15] Later, using a time-dependent perturbation theory result,[55] they wrote down a TCF expression for the SFG signal and evaluated it in terms of a TCF of the systems coordinates in the linear dipole and Placzek approximation; their expression appears to be correct only for the modulus of the signal.[6]

8.1. Theoretical Frequency Domain Approaches to the SFG Spectrum

8.1.1. Applications to the Water/Vapor Interface

The next theoretical study was due to Morita and Hynes and examined the O−H stretching region of the ambient water/vapor interface. They adopted a frequency domain approach that was highly effective.[5,15] Their method was reminiscent of a very similar approach to calculating the IR spectrum of bulk water that was employed earlier.[129−131] To calculate the SFG spectrum, the authors evaluated the perturbation expression for the susceptibility[24] for harmonic normal mode, Q:

$$\chi_R^{(2)}(\omega_{SFG}) \propto (\partial\mu_i/\partial Q)\,(\partial\alpha_{jk}/\partial Q)\left[\frac{\omega_{SFG}-\omega_{IR}}{(\omega_{SFG}-\omega_{IR})^2+\gamma^2}\right] \quad (47)$$

$$\chi_{\mathrm{I}}^{(2)}(\omega_{\mathrm{SFG}}) \propto (\partial\mu_i/\partial Q)\,(\partial\alpha_{jk}/\partial Q)\left[\frac{\gamma}{(\omega_{\mathrm{SFG}}-\omega_{\mathrm{IR}})^2+\gamma^2}\right] \tag{48}$$

Equations 47 and 48 present the real and imaginary parts of the susceptibility where γ is a mathematical convergence parameter that physically can be interpreted as a homogeneous line width and was estimated in their work. Note that the choice of γ has a large effect on the signal shape. Equations 47 and 48 demonstrate that the signal magnitude is proportional to the product of dipole and polarizability derivatives, which provides the interface specificity. The equations can then be evaluated for each molecule's normal coordinates in the molecular frame and rotated into laboratory coordinates. The different molecular contributions are then summed for an ensemble of configurations.

To calculate the nature of the (bulk and) interfacial normal coordinates, it was assumed a priori that the O−H stretching modes were localized on single molecules—this had been demonstrated theoretically for the bulk O−H stretching modes earlier.[100,129,130] Next, the mode shapes were calculated based on a water molecule's local environment. The O−H stretching mode was taken as a linear combination of the gas phase symmetric and antisymmetric stretching modes with weights based on a simple two state vibrational eigenvalue equation that included a calculation of the condensed phase O−H frequency shift (calculated by using the force on the bond coordinate and a cubic anharmonic potential function parametrized to ab initio calculations) and the off diagonal gas phase mode couplings. The polarizability and dipole derivatives are then calculated by parametrizing the derivatives as a function of O−H bond length using ab initio calculations.

Finally, the SFG intensity was calculated by multiplying the squared modulus of the susceptibility by the frequency squared, in accordance with eq 15. The nonresonant contribution was assumed to be a constant.[5,19] The resulting SFG spectrum in the SSP geometry for the ambient water/vapor interface is presented in Figure 8 (the paper also presents the SPS spectrum). The resulting line shape compares quite favorably to the experimental measurement in Figure 7a and displays the essential features with a free O−H stretching mode at about 3700 cm^{-1} and a broad somewhat structured signature between about 3000 and 3600 cm^{-1}. This method is appealingly (relatively) simple and was successfully adopted by experimentalists to model other aqueous interfaces.[12,122]

Interestingly, this methodology can be interpreted as an approximation to instantaneous normal mode (INM) methods to calculating spectra,[1−3,101,124,125,137−150] in which the relevant perturbation expression is also evaluated for harmonic oscillators. The difference in the INM approach is that the normal modes are calculated as the exact normal coordinates of the instantaneous configuration of the system, and the homogeneous line width is neglected (it is effectively the bin size used to calculate the spectrum to approximate a δ function contribution). The results from the Morita and Hynes work are, however, different from the INM results,[2,3] which are consistently broader (even though their work uses a relatively large line width of $\gamma = 22$ cm^{-1}).[5] This implies that the method used to calculate the frequency shifts must not sample all of the underlying frequency fluctuations and effectively includes some motional narrowing thus giving a spectrum resembling that which is observed experimentally.

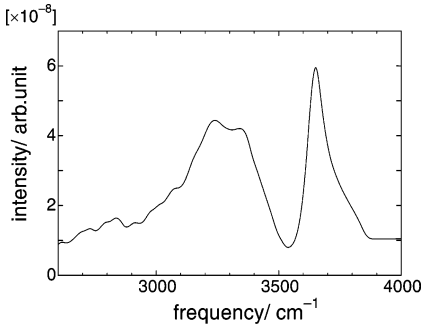

Figure 8. Simulated SFG spectrum of water of SSP polarization using a frequency domain method. Reprinted with permission from ref 5. Copyright 2000 Elsevier.

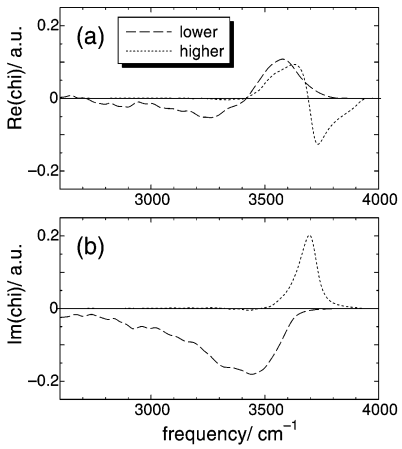

Figure 9. Susceptibility $\chi_{\mathrm{SSP}}^{\mathrm{res}}$ per unit surface area decomposed into two vibrational eigenstates: lower energy state (− − −) and higher energy state (•••). Panels a and b show the real and imaginary parts, respectively. Reprinted with permission from ref 5. Copyright 2000 Elsevier.

Results from INM spectroscopy calculations of SFG spectra will be considered in more detail below, but INM methods do show that the interfacial normal modes are largely localized on single molecules consistent with the ansatz used in the above work.[1−3] Their study also plotted the real and imaginary parts of the susceptibility, shown in Figure 9, which is due to the upper and lower vibrational eigenstates from each molecule.[5] Note that it was also found that the eigenstates are approximately O−H local stretching modes although the lower (higher) frequency modes show symmetric (antisymmetric) mode character; this is consistent with results from INM studies both at the interface[1,3] and in the bulk.[101] Figure 9 demonstrates that the higher frequency mode is largely responsible for the free O−H stretch and the lower eigenstate on the same molecule makes up most of the rest of the O−H stretching spectrum. This evidence is consistent with an interpretation of the O−H stretching spectrum as a free O−H and donor O−H region. However, it will be shown below, by analyzing the real and imaginary parts of the susceptibility (on a better averaged signal) in more detail, that the donor O−H region apparently contains a number of distinct oscillator species.[3,19,22]

Figure 10 is from the same work and represents the first theoretical investigation of the interface specificity of the SFG signal. It is clear that the free O−H stretches are nearly all localized at the interface and the donor O−H region of the spectrum has a dominant contribution from the first layer of molecules yet exhibits nonnegligible intensity from the second layer. The ability to describe an SFG signal in

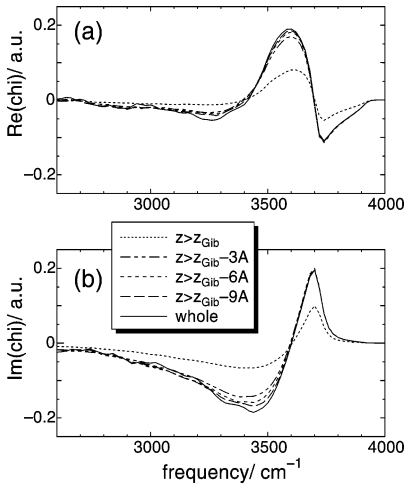

Figure 10. Surface sensitivity of the susceptibility χ^{res}_{SSP} per unit surface area of water. The solid lines denote the whole susceptibility, and the other lines correspond to virtual susceptibilities within restricted systems by various depths from the surface to examine the convergence. Panels a and b show the real and imaginary parts, respectively. Note that the depths are given with respect to the calculated Gibbs dividing surface. Reprinted with permission from ref 5. Copyright 2000 Elsevier.

molecular detail is a significant strength of SFG spectroscopy.

8.1.2. Applications to Other Aqueous Interfaces

Using the theoretical frequency domain techniques described by Morita and Hynes, Brown et al. examined the hexane/water and CCl_4/water interfaces.[12] The simulated SFG spectra for these interfaces are in excellent agreement with the experimental spectra. In both systems, a sharp free O−H peak is observed at ≈3700 cm^{-1} as well as a broad peak at ≈3400 cm^{-1}. The relative intensities are comparable to experiment for both interfaces.

Comparison of the two systems reveals that the frequency of the free O−H vibration is slightly lower for the CCl_4/water and hexane/water interface than for the water/vapor interface due to interactions at the interface between either CCl_4 or hexane and water. The intensity of the free O−H peak is significantly decreased in the hexane/water spectra as compared to the CCl_4/water interface and is speculated to be due to strong interactions between the free O−H oscillators at the interface and hexane. This interaction is also postulated to be the cause of some asymmetry in the free O−H peak for the hexane/water interface.

8.2. Theoretical Time Domain Approaches to the SFG Spectrum

The remaining theoretical SFG studies all adopted a time domain approach[1−4] to calculate the resonant susceptibility similar to that introduced originally by Girardet.[6] All of these approaches require, at their core, calculating the cross TCF of the system dipole and polarizability, $\langle \alpha_{pq}(t)\, \mu_r(0) \rangle$. This, being the product of a first and second rank tensor, vanishes in isotropic media.[151] The following derivation follows that of Perry et al. The resonant part of the susceptibility is given by the imaginary part of this quantum mechanical TCF via eq 31. The goal, in this context, is to rewrite eq 31 in a form that is amenable to calculation using classical TCF theory in order to take advantage of the power of the molecularly detailed description offered by many body classical MD. To proceed, the imaginary part of the one time TCF is related in frequency space exactly to the real part: $C_I(\omega) = \tanh(\beta\hbar\omega/2)\, C_R(\omega)$, where the subscripts denote the Fourier transform of the real and imaginary parts of the complex function $C(t)$, which is a real function of frequency, i.e.,

$$C(\omega) = (1/2\pi) \int \int_{-\infty}^{\infty} \mathrm{d}t\, e^{-i\omega t} [C_R(t) + iC_I(t)] = C_R(\omega) + C_I(\omega)$$

Substituting into eq 31 gives

$$\chi^{res}(\omega) = \frac{2}{\hbar} \int_0^{\infty} \mathrm{d}t\, e^{i\omega t} C_I(t)$$

$$C_I(t) = \int_{-\infty}^{\infty} \mathrm{d}\omega'\, e^{i\omega' t} \tanh(\beta\hbar\omega'/2)\, C_R(\omega') \quad (49)$$

Note that $C_I(t)$ is written in a form that can be calculated using the real part of the correlation function, which is approximately obtainable, after quantum correction, using classical MD and TCF approaches. Because of causality, the Fourier−Laplace transform gives a real and imaginary part in eq 49 as the cosine and sine transform of $C_I(t)$, respectively. Equation 49 can be simplified by changing the order of integration—performing the frequency domain integral first. Defining the real and imaginary parts of $\chi^{res}(\omega) = \chi^{res}_R(\omega) + i\chi^{res}_I(\omega)$:

$$\chi_I(\omega) = \frac{1}{\hbar} \tanh(\beta\hbar\omega/2)\, C_R(\omega) = \frac{2}{\hbar} \int_0^{\infty} \sin(\omega t)\, C_I(t)\, \mathrm{d}t \quad (50)$$

$$\chi_R(\omega) = \frac{1}{\pi\hbar} P \int_{-\infty}^{\infty} \frac{\tanh(\beta\hbar\omega/2)\, C_R(\omega')}{\omega + \omega'} \mathrm{d}\omega' = \frac{2}{\hbar} \int_0^{\infty} \cos(\omega t)\, C_I(t)\, \mathrm{d}t \quad (51)$$

To obtain eqs 50 and 51, the identity $\int_0^{\infty} e^{i\omega t}\, \mathrm{d}t = iP/\omega + \pi\delta(\omega)$ was used. P designates the principle part.[95]

The current focus of SFG experiments is on intramolecular vibrations, and to calculate observables in this spectral region, classical mechanics is clearly invalid. Building on our previous work, the classical correlation function result, which is amenable to calculation using MD and TCF methods, is quantum corrected using a "harmonic correction" factor: $C_R(\omega) = C_{Cl}(\omega)\, ((\beta\hbar\omega/2)\, \coth(\beta\hbar\omega/2))$.[107,152] This correction factor is exact in relating the real part of the classical harmonic coordinate correlation function to its quantum mechanical counterpart. It is worth noting that it is not uncommon in modeling vibrational spectroscopy via TCFs to see the real part of the quantum TCF replaced by the classical TCF that has the same even time symmetry and becomes equivalent classically (at low frequencies where $\hbar\omega \ll kT$). This approach is reasonable in describing vibrational line shapes but does not give accurate intensities. It is generally better to use the harmonic correction factor. Similar caveats apply to replacing the full quantum TCF with its classical counterpart, but in that case, one neglects the imaginary part of the TCF entirely (that may not matter very much when considering high-frequency phenomena for which $C_I(\omega) = C_R(\omega)$ because the hyperbolic tangent function is approaching unity).

Using the classical harmonic coordinate quantum correction factor does not account for the fact that the dipole and polarizability contain higher orders of the coordinates—exact corrections for harmonic systems of this type are still possible but unneeded (the linear dipole and Placzek approximation are adequate).[107] Using this result, the TCF approximation to the resonant part of the SFG spectrum, χ^{res}, takes the form:

$$\chi_I(\omega) = \beta\, \omega\, \pi\, C_{Cl}(\omega) \tag{52}$$

$$\chi_R(\omega) = \beta P \int_{-\infty}^{\infty} \frac{C_{Cl}(\omega')\, \omega'}{\omega + \omega'}\, d\omega' \tag{53}$$

$$C_{Cl}(t) = \langle\, \mu_i\,(0)\, \alpha_{jk}\,(t)\, \rangle \tag{54}$$

In eq 54, the angle brackets represent a classical TCF that can be computed using MD and a suitable spectroscopic model.[4,153] Finally, eqs 52 and 53 give the TCF signal in a form amenable to classical simulation. Note that while it easier to evaluate $\chi_I(\omega)$ using eq 52, $\chi_R(\omega)$ is more easily computed by doing the cosine integral as in eq 51.[3] Considering three possible independent polarization conditions, SSP, PPP, and SPS, for the TCF in eq 54, the first index in the polarization designation corresponds to the last index in the TCF. For example, the SSP and PPP polarization conditions probe dipolar motions normal to the interface, and the SPS case is sensitive to dipolar changes parallel to the interface. Note that the PPP condition is sensitive to motions both parallel and perpendicular to the interface.[78] Furthermore, the (SSP and PPP)/(SPS) probes diagonal/off diagonal polarizability matrix elements, respectively.

Morita and Hynes adopted a very similar approach to modeling the SFG spectrum, but quantum corrections were not included. Additionally, the RWA was invoked (see section 7.1). The RWA is equivalent to setting the hyperbolic tangent factor to unity in eq 49. At lower frequencies, including this factor leads to expressions that are quite different, and the tanh factor produces a time derivative of the correlation function in the time domain.

Perry et al. also constructed an INM approximation to SFG spectra. To do so, it is sufficient to evaluate eqs 52−54 for a harmonic system. To do so, it is convenient to invoke both the Placzek and the linear dipole approximation to evaluate the resulting matrix elements (consistent with the frequency domain work in section 8.1),[5] although higher order contributions can be included and simple analytic expressions result for these contributions. An equivalent approach is to evaluate $C_{Cl}(t)$ for classical harmonic oscillators and quantum correct the resulting expression using the harmonic correction factor, given above, to relate $C_{Cl}(t)$ and $C_R(t)$.

$$C_{Cl}(\omega) = \left\langle\, (\partial\mu_i / \partial Q_l)\, (\partial\alpha_{jk} / \partial Q_l)\, \delta(\omega - \omega_l)\, \frac{kT}{\omega^2} \right\rangle \tag{55}$$

In eq 55, ω_l is the frequency of mode Q_l and the angle brackets represent averaging over classical configurations of the system. $C_{Cl}(\omega)$ is then back transformed into the time domain and used in eqs 52 and 53 in place of the classical TCF to obtain an INM approximation to the spectroscopy.

8.2.1. Applications to the Water/Vapor Interfaces

The first application of TCF theory to water vapor interfaces was by Morita and Hynes[4] followed by a study by Perry et al.[1] Both investigations concentrated on the O−H stretching region of the SSP SFG spectrum. To calculate the requisite TCF in eq 54, it is necessary to first create a series of time-ordered MD configurations of the interface using a particular force field. Morita and Hynes employed both polarizable and nonpolarizable models while Perry et al. used a (nonpolarizable) flexible simple point charge[132] model. In calculating the TCF itself, a spectroscopic model is needed to calculate the time-dependent dipoles and polarizabilities. Calculating accurate TCFs for SFG spectroscopy is difficult because not only is accurate calculation of the dipoles and polarizabilities required but is also essential to properly describe their derivatives, which control intramolecular intensities. Morita and Hynes used a spectroscopic model based on extensive ab initio calculations to describe the change of the dipole and polarizability in the gas phase and a bond polarizability description of the many body polarization contributions in the condensed phase. Perry et al. used a many body polarization model (a point atomic polarizability model)[154−157] for the polarizability and induced dipoles that naturally incorporates the polarizability derivatives (fit to both ab initio and experimental Raman data).[158,159] The considerations in choosing a spectroscopic model are no different from those required for modeling condensed phase Raman or IR spectra and need not be repeated here.

Unfortunately, these early TCF studies produced very noisy spectra that were difficult to interpret because evaluating the TCF in eq 54 presents a problem for interfacial systems; MD interfaces are typically constructed using a standard MD geometry with vacuum/vapor above and below the water.[5,9] This produces two interfaces with average net dipoles in opposite directions. Calculating the SFG spectrum of the entire system would lead to partial cancellation of the SFG signal and meaningless results. Therefore, the system needs to be split into two pieces through the center of mass of the interfacial system along the direction normal to the interface. Each of the resulting subsystems is then handled separately, and each molecule is assigned to one-half or the other for the entire length of the calculation.

Still, a problem arises in that molecules at one interface can diffuse to the other interface over time. This is a problem in calculating the TCF spectra where different molecular contributions are all added to form a single net dipole and polarizability at each step that are then correlated to form $C_{Cl}(t)$.[153] Using the bulk diffusion constant for water, it can be estimated that it takes about 30−50 ps for a molecule to diffuse from one interface to the other for the system sizes considered. It was, therefore, necessary to limit the length of a TCF correlation time to 15 ps (for 108 particles) or 30 ps (for 512 particles), and many correlations of this length were performed in calculating an averaged TCF.

The need to do this can be understood from a single molecule perspective. If cross-terms between the dipoles and the polarizability elements could be neglected, $C_{Cl}(t)$ could be written in terms of single molecule contributions: $C_{Cl}(t) \approx N\, \langle\, \mu_i^M(0)\, \alpha_{jk}^M(t)\, \rangle$, where N is the number of molecules and the superscript M is the molecule index.[96] Because bulk isotropic molecular motions give no SFG signal, it is the anisotropic dynamics of molecules at the interface that generate a signal. Both the polarizability tensor elements and the dipole moment are independent of translational origin; thus, it is only necessary to distinguish between molecules exhibiting bulk and interfacial dynamics to understand the contribution of a molecule to the TCF. If a molecule were to reside at both interfaces during the duration of the TCF

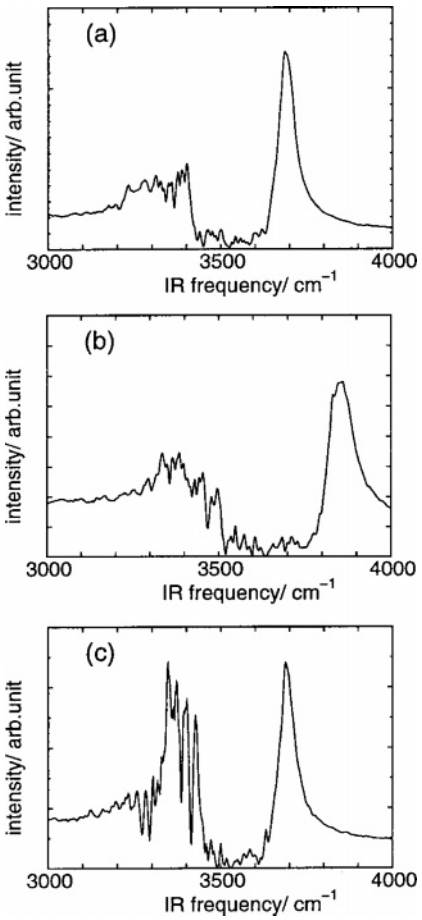

Figure 11. Calculated SSP SFG spectrum of the water surface. Three models are employed: (a) the Ferguson force field with no induced polarization, (b) the Kuchitsu and Morino force field with no induced polarization, and (c) the Ferguson force field with induced electronic polarization. Reprinted with permission from ref 4. Copyright 2002 American Chemical Society.

calculation, invalid results would be obtained. Furthermore, if molecules were reassigned to a specific half of the system at each calculation time point, an asymmetry would be introduced at the dividing surface by including the dynamics of a molecule at only certain steps as it appears in, and disappears from, a given half. This would introduce an artificial inhomogeneity in truly bulklike isotropic dynamics that might generate an SFG signal.[1] The fact that the correlation function calculations were limited to short times and the SFG TCF, a cross-correlation between the system dipole and the polarizability elements (not invariants such as in traditional Raman and IR experiments), is long-lived leads to poor averaging at longer times. This makes the signal difficult to accurately Fourier transform even though the focus is on extracting the short time high-frequency behaviors. Nonetheless, the spectra that were obtained resembled the experimental data and clearly showed a free O−H and donor O−H region. Figure 11 presents the TCF-generated spectra for three distinct MD models.[4] It is clear that while the free O−H peak is relatively well-averaged, the rest of the O−H spectrum is not sufficiently well-resolved to reveal its structure. The author's do note that the polarizable MD model produces relative intensities between the two regions of the spectrum reminiscent of the experimental results. Perry et al.[1] present similar results but erroneously conclude (largely due to the noisy data) that dynamical effects (motional narrowing) are not represented in the SSP spectrum; this result is strongly contradicted by their later work discussed below. Their approach was to compare INM- and TCF-generated spectra. INM results represent an underlying spectral density that may or may not be motionally narrowed in the observed line shape.[3,54,101] If the INM and TCF spectra are similar in breadth (and in that case in shape), then dynamical effects will not be represented in the line shape. When dynamical effects are important, the INM line shape will be broader but, in both cases, will have the same integrated intensity. The author's also show an INM illustration of a representative free and donor O−H on a single molecule demonstrating the power of the INM approach in revealing the molecular nature of vibrational modes.[1]

To obtain better TCF results, long time (cross) correlations between the system dipole and the polarizability need to be followed. To overcome the time limit problem discussed above, Perry et al.[2,3] added a weak (laterally isotropic) restraining potential on the oxygen atoms to the MD force field that effectively confined molecules over time to the half of the simulation box that they start in (in the dimension normal to the interface). The external potential was chosen such that it did not significantly perturb the relevant dynamics; even though the molecular diffusion constant (normal to the interface) is changed, the molecule can only contribute to the spectrum while resident at the interface where it is free of any significant external potential. This modification permitted the calculation of TCFs out to arbitrarily long times resulting in sharp spectra that included intermolecular spectral line shapes. As a check, it was noted that the interfacial density profile and orientational structure were unchanged by the restraining potential, demonstrating that the restraining potential used did not perturb the average structure of the liquid that contributes to the interfacial spectroscopy.

Figure 12 displays the theoretical TCF SFG spectra in the O−H stretching region for the three independent polarization conditions that are possible in the electronically nonresonant experiment (SSP, PPP, and SPS) when the TCFs were converged at long times.[2] The theoretical spectra have been adjusted in relative intensity to account for the Fresnel factors that modify the experimental intensities to directly compare with experiment;[3,14] the data also include the nonresonant contribution, $\chi^{Nres}(\omega)$, which is a small negative constant.[4,134] The full signal is given by $|\chi^{(2)}_{SFG}(\omega)|^2 \propto |\chi^{res}(\omega) + \chi^{Nres}(\omega)|^2$.

The inset of Figure 12 displays experimental data for the O−H stretching region taken in the same polarization geometries.[14] The relative intensities agree nearly quantitatively between theory and experiment, and the line shapes are far improved over the earlier attempts.

Because of the use of the restraining potential and the ability to follow the TCF out to long times, the authors were able to obtain, for the first time either experimentally or theoretically, low-frequency SFG spectra. Figure 13 displays the theoretical SFG spectrum over the entire water vibrational spectrum.[2] The theoretical INM spectrum (for the SSP geometry) is also shown. The INM and TCF spectra were found to integrate to the same value (over the entire 0−5000 cm^{-1} range) and separately over the O−H stretching region (2000−5000 cm^{-1}). This behavior is strong evidence for the interpretation of the INM line shape as an underlying spectral density that is motionally narrowed in the observed spectrum. This result also suggests that SFG spectra are sensitive to both structure and dynamics. The INM spectrum clearly

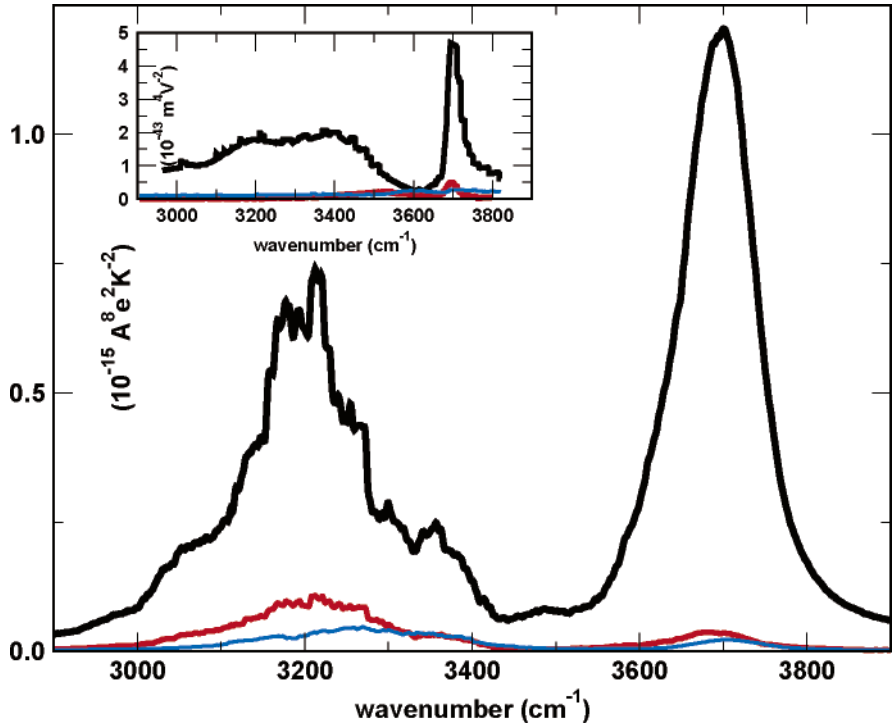

Figure 12. TCF SFG spectra in the O−H stretching region for three polarizations: SSP (black line), PPP (red line), and SPS (blue line). The inset is experimental data[14] for the same polarizations using the same color scheme. Reprinted Figure 1 with permission from ref 2 (http://link.aps.org/abstract/PRE/v71/e050601(1)). Copyright 2005 by the American Physical Society.

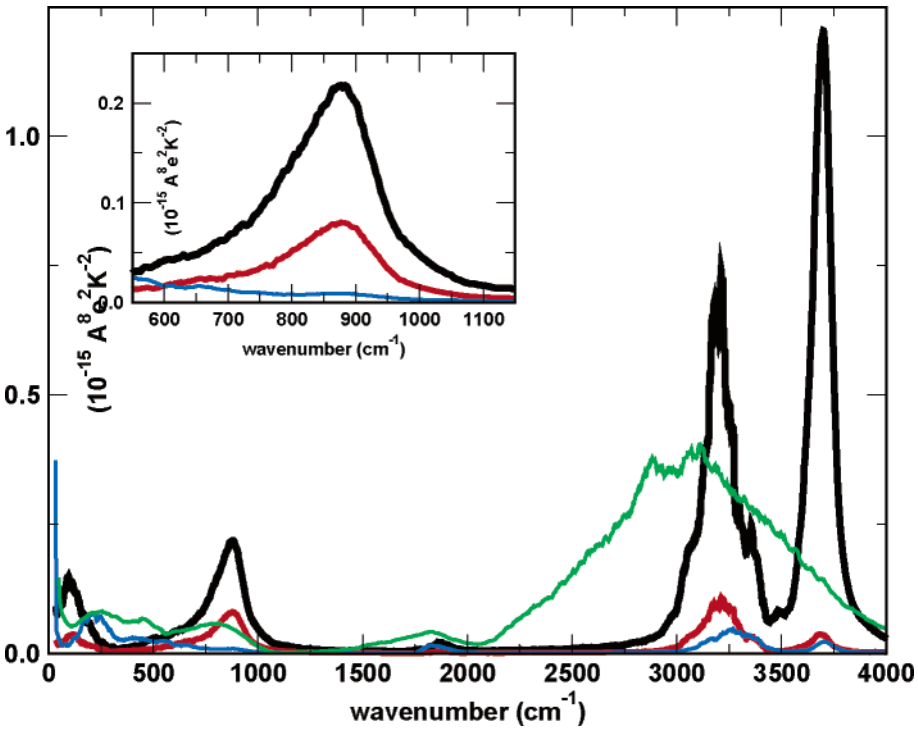

Figure 13. TCF SFG spectra for the entire water vibrational spectrum for three polarizations: SSP (black line), PPP (red line), and SPS (blue line). The SSP INM SFG spectra is also shown (green line). The inset highlights the intermolecular resonance at 875. cm^{-1}. Reprinted Figure 2 with permission from ref 2 (http://link.aps.org/abstract/PRE/v71/e050601(1)). Copyright 2005 by the American Physical Society.

exhibits the same resonances but is broader, implying that the observed line shapes are motionally narrowed and dynamical contributions to SFG signals are important.[3,14]

Most strikingly, Figure 13 reveals an intense intermolecular resonance at 875 cm^{-1}. In contrast, the intermolecular spectrum of bulk water is relatively unstructured.[101] This symmetric line shape indicates a spectroscopically distinct species and represents—like the free O−H stretch—a population of water molecules unique to the interface. It is roughly as intense (considering the susceptibility and not the SFG intensity that includes an additional factor of the frequency squared) as the rest of intermolecular spectrum and is about a sixth of the intensity of the free O−H peak within our model. (Note that the bending line shape at higher frequency

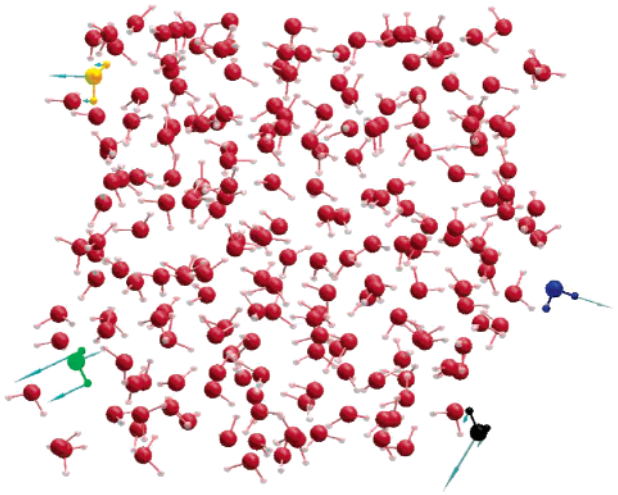

Figure 14. Snapshot of a water/vapor interface containing 216 water molecules featuring INMs from different regions of the spectra. The water molecule shown in blue is representative of a free O−H mode at 3694 cm^{-1}. The water molecule shown in green is representative of a wagging motion at 858 cm^{-1}. The water molecule shown in yellow highlights a translation perpendicular to the interface at 46 cm^{-1}. The water molecule shown in black highlights a translation parallel to the interface at 197 cm^{-1}.

is much less intense.) Recent experiments[42,43] and theory[7] indirectly inferred the presence of a surface species—a water molecule with two dangling hydrogens.

The SSP and PPP spectra also show an intense intermolecular mode at 95 cm^{-1}. Using INM methods, the resonance was found to be due to hindered translational modes localized on single molecules oscillating perpendicular to the interface. The SPS spectra, which are sensitive to dipole derivatives parallel to the interface, show an intermolecular mode at 220 cm^{-1}. This mode is a result of translations parallel to the interface. These results highlight the importance of polarization sensitivity in SFG experiments. The authors also note that these species could be experimentally measurable using SFG, but this has not been done to date due to a lack of intense IR laser sources in this spectral region. The fact that these interfacial species have gone long undetected might be surprising given the large numbers of MD simulations of the water/vapor interface that have been performed previously. This observation highlights the power of calculating spectroscopic observables in assessing interfacial structure and dynamics. Not only can the results be directly compared with experiment—thus, validating a particular MD and spectroscopic model—but also the spectroscopic calculation serves as a filter of the dynamics extracting out the identity of collective coordinates with well-defined frequencies that persist at the interface. The authors also show an MD-generated "snapshot" of the interface, which is detailed in Figure 14. This molecular snapshot highlights the different interfacial species that were identified in their studies.[3] The hindered rotational (wagging) and translational modes are clearly shown. These results demonstrate how the INM approach does not require a priori assumptions about the nature of interfacial modes but does reveal their physical characteristics and how different molecular motions contribute to the spectrum.

It was also observed that examining the real and imaginary parts of the spectrum can offer insights unavailable from the modulus alone.[3] The real and imaginary parts could be measured experimentally via a heterodyne detection scheme

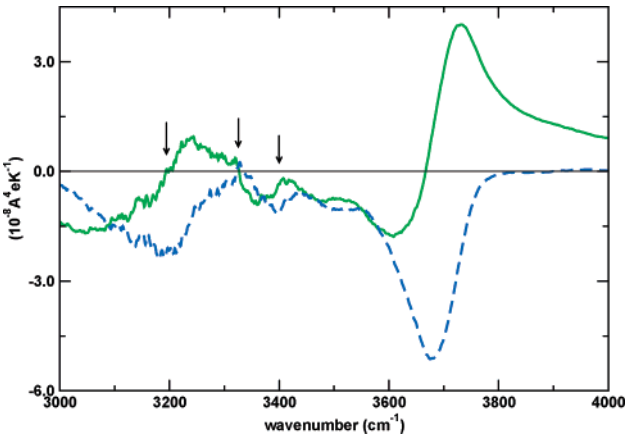

Figure 15. Real (solid green line) and imaginary (dashed blue line) components of the SFG SSP TCF spectra for the water/vapor interface for the O−H stretching region. The arrows highlight three separate modes centered at 3195, 3325, and 3400 cm^{-1}.

or by taking advantage of interference effects between bulk and interfacial contributions to the spectrum.[16] To see the advantages of separately examining the real and imaginary contributions, it is useful to reexamine eqs 47 and 48. They imply that a single type of mode will lead to an imaginary contribution that is a symmetric well-defined peak (Lorentzian in character) while the real part will change sign, dipping below zero, at the maximum of the imaginary portion. If more than one species is contributing to the signal in a given region, a more complex line shape would result from the overlapping signals. As pointed out by Morita and Hynes,[5] orientational information can also be deduced from the relative signs of the imaginary mode line shapes given knowledge of the signs of the prefactors in eqs 47 and 48 (the dipole and polarizability derivatives).

Figure 15 presents the real and imaginary parts of the susceptibility in the O−H stretching region, from approximately 3000 to 3600 cm^{-1} calculated by Perry et al.[3] Careful examination of the spectrum reveals three separate modes in this region centered at 3195, 3325, and 3400 cm^{-1}. Remarkably, this agrees very well with previous experimental work that deconvoluted the spectrum in this region. That analysis revealed three modes present in the same region centered at 3200, 3325, and 3454 cm^{-1}—nearly the same frequencies as shown in Figure 7.[19,134] This is strong evidence for distinct populations of water molecules in this donor O−H region of the spectrum. These results represent strong motivation for experimentalists to measure the real and imaginary parts of the susceptibility for the water/vapor interface.

8.2.2. Applications to Saltwater/Vapor Interfaces

Interfacial electrolytes are import in biological, industrial, and atmospheric processes. Despite the importance of these interfaces, the atomic details of the surface of electrolyte solutions are unknown. Recent theoretical and experimental work, including SFG studies, by Jungwirth, Tobias, Allen, and co-workers has shed some light on the interfacial composition at simple inorganic salt solutions.[11,18,160−162]

Historically, the view has been that the interface is largely devoid of ions. This view comes from thermodynamic arguments and experimental evidence such as surface tension measurements.[163,164] The argument is that differences between

the bulk and the interfacial concentrations can be related by the Gibbs equation and also by considering the concept of Gibbs surface excess (when the interfacial region's density is not constant). The Gibbs equation relating surface tension to surface excess is given by:

$$\Gamma = -\beta\left(\frac{d\gamma}{d \ln c}\right) \quad (56)$$

In eq 56, Γ is the surface excess, γ is the surface tension, β is $1/k_bT$, and c is the concentration.[163,164] Using this treatment, a decrease in surface tension (relative to the pure substance) results from an increase in concentration at the interface (e.g., due to surfactants), and an increase in surface tension results from a decrease in concentration at the interface. Thus, because simple inorganic salts, such as aqueous NaCl, increase the surface tension relative to pure water, a decrease in concentration at the interface is inferred. These thermodynamic arguments have been used for almost a century to conclude that when considering simple salt solutions, their interfaces will be nearly devoid of ions.

Recent theoretical[11,18,160,161,165,166] and sensitive experimental[18,134,167−169] work have called this traditional view into question, specifically, the pioneering work of Jungwirth and Tobias[166] that predicted a surface enhancement of chloride ions at the solution/vapor interface for aqueous salts. Recent theoretical work has suggested that the propensity for surface enhancement depends on the polarizability and size of ion; the larger and more polarizable the ion, the bigger the surface concentration enhancement will be. For example, the relatively small and weakly polarizable F^- is repelled from the surface consistent with the traditional view. Conversely, Cl^-, Br^-, and I^-, all large polarizable ions, show enhancement at the interface. The simulations that displayed this enhancement employed polarizable force fields in contrast to earlier simulation studies using traditional nonpolarizable forces. Consequently, if the aqueous anion is not treated with a polarizable model during the simulation, enhancement of the anion at the surface is diminished or eliminated.

Enhancement in interfacial concentration of the more realistically modeled polarizable anion is not in contradiction with the thermodynamic equations because these equations allow for a nonmonotonic ion concentration profile.[160] Indeed, the simulations suggest an overall net decrease of the ion concentration, in agreement with the thermodynamics, with a corresponding increase in surface tension. However, the profile is not monotonic; there is an increase in concentration relative to the bulk at the outermost layer and a depletion relative to the bulk just below the surface to give an overall depletion of the ions at the interface.

Because SFG is a sensitive probe of the interface, Brown et al.[11] have calculated the SFG spectra arising from salt ($NaI_{(aq)}$) air interfaces to look for a signature characteristic of anions at the solution/vapor boundary. They calculate the SFG spectrum of the $NaI_{(aq)}$ interface using a time domain approach but without the advantages of a restraining potential.[4] I^- was chosen as the anion because it showed the largest interfacial enhancement in previous simulations.[160] The authors were not able to obtain a reasonable frequency-independent nonresonant susceptibility and, thus, scaled their neat water results to match what has been previously reported. They subsequently used these same scaling factors to deduce the interfacial spectra of the salt solution. Because of these scaling factors, the authors did not compare or draw absolute conclusions from the computed spectra but did compare and contrast the neat water/vapor spectra with the saltwater/vapor spectra.[11]

The $NaI_{(aq)}$/vapor-calculated SFG spectrum differs in several ways from the neat water/vapor spectrum that was obtained. Relative to the neat interface signal, there is a slight decrease in the free O−H peak at about 3750 cm^{-1}, a large increase in the peak near 3400 cm^{-1}, and a slight decrease in the shoulder peak at 3250 cm^{-1}.

SFG experimental results on the $NaI_{(aq)}$/vapor SFG and other sodium halides have been reported by Raymond and Richmond[134] and independently by Liu et al.;[168] both show similar spectra. These spectra are qualitatively similar to the SFG spectra calculated by Brown et al.[11] but differ in the details. Both experiment and simulation show little difference in the free O−H peak (as compared to the neat interface), a large increase in the peak at about 3400 cm^{-1}, and a slight decrease in the shoulder peak at 3250 cm^{-1}. However, the relative changes in intensity are different between the experimental and the simulated spectra. Furthermore, while the reported experimental spectra are very similar for the two groups, they interpret their data differently. Raymond and Richmond ascribe the difference between the neat water/vapor and the saltwater/vapor interface as evidence that the anion is in the subsurface region. In contrast, Liu et al. interpret the observed spectral changes as evidence that the anion is at the surface—similar to the MD simulations.

Recently, Mucha et al. have reported simulations and experimentally measured SFG signals of acid, base, and salt solutions.[18] While the SFG signal for these systems has not been calculated, the experimental SFGs are interpreted in terms of the extant ionic solution simulations. Using the methods outlined in this review, improvement in agreement between the computed and the experimentally measured SFG spectra for the salt solution/vapor interface seems likely. Such calculations will allow for the confident interpretation of the spectra and atomistic resolution of the interfacial region of these important electrolyte systems.

9. Conclusion

SFG experimental measurements are growing in number and importance; they are providing valuable information about interfacial structure and dynamics that would be difficult to measure or are not obtainable otherwise. Theoretical studies are only now sufficiently sophisticated that they can begin to play the major role simulation has in modeling and interpreting condensed phase spectroscopy. In principle, SFG spectroscopy is capable of giving a complete picture of the interface, including structure and dynamics (although fourth order polarization experiments[170−172] would be required to analyze the detailed interface vibrational dynamics and unambiguously distinguish between homogeneous and inhomogeneous vibrational line shapes).[55] Realizing this promise depends critically on the spectra being reliably interpreted, and the methods described in this review are capable of unambiguously characterizing the nature of SFG spectra, including inferring subpopulations of molecules from complex line shapes. Still, a vigorous interplay between theory and experiment is needed to further develop the interpretative and predictive power of theoretical studies. The investigation of more complex interfaces using the improved TCF methods, described here, will help both to interpret the large and growing body of experimental data and to predict heretofore unexplored interfacial vibrational structure. Fur-

thermore, experimental advances are likely to extend the frequency range for SFG measurements into the far IR where theory predicts that important interfacial species are present; lower frequency phenomena are important in contributing to processes such as interfacial solvation reaction dynamics.

Additionally, time domain SFG techniques are extending the abilities of SFG spectroscopy to probe interfacial vibrations in new novel ways. However, these methods require theoretical support in designing and interpreting the convoluted signals that result. Last, theoretical and experimental measurements of both the real and the imaginary parts of the SFG signal (as opposed to measuring the squared modulus as in the typical homodyne detected experiment) show great promise in helping unravel complex SFG line shapes. It would be beneficial to the field if more experiments were conducted (either via heterodyne detection or use of interference effects) to separately measure these contributions.

10. Acknowledgments

The research at USF was supported by an NSF Grant (CHE-0312834), a grant from the Petroleum Research Foundation to B.S., and a Latino Graduate Fellowship to C.N. Acknowledgment is made to the Donors of the American Chemical Society Petroleum Research Fund for support of this research. We acknowledge the use of the services provided by the Research Oriented Computing Center at USF. We also thank the Space Foundation for Basic and Applied Research for partial support. We also thank Drs. Alex Benderskii, Chris Cheatum, Zhan Chen, Randy Larsen, and Tom Keyes for helpful discussions. Last, we thank Christina Ridley Kasprzyk and Tony Green for their contributions to the work.

11. Appendix A: Possible Second-Order Nonlinear Processes

For three-wave mixing experiments, there are two relevant applied time-dependent fields, which result in a sum of $(2N)^N = 16$ terms when specific time ordering of the fields cannot be assumed. Each one of these 16 pathways corresponds to a specific $\mathbf{P}^{(2)}(\mathbf{k}_s, t)$. Of the 16 possible contributions, only four distinct physical processes occur, SFG, DFG, SHG, and optical rectification. Each of the four effects can be independently measured experimentally using the appropriate phase matching condition that corresponds to a particular experimental geometry and associated signal wave vector, $\mathbf{k}_s$.[55,57]

Note that for SHG experiments, where two visible fields of the same frequency are typically used, four of the pathways (and their complex conjugates) become equivalent providing added intensity. SHG experiments are also extensively used to probe interfacial properties when a chromophore is present that can be excited by the visible light.[173−176]

Table 1. Possible Second-Order Nonlinear Optical Processes Given in Terms of the Incident Wave Vectors

SHG	$\mathbf{k}_s = \pm 2\,\mathbf{k}_i$	$\omega_s = \pm(\omega_i + \omega_i)$
SFG	$\mathbf{k}_s = \pm(\mathbf{k}_1 + \mathbf{k}_2)$	$\omega_s = \pm(\omega_1 + \omega_2)$
DFG	$\mathbf{k}_s = \pm(\mathbf{k}_1 - \mathbf{k}_2)$	$\omega_s = \pm\omega_1 \mp \omega_2$
optical rectification	$\mathbf{k}_s = 0$	$\omega_s = 0$

Table 2. Column 1 Details the 16 Terms Resulting from the Two Incident Fields, and Column 2 Gives Their Corresponding Nonlinear Optical Process, Respectively

$\mathbf{E}_1(t-\tau_1)\,e^{i\mathbf{k}_1\cdot\mathbf{r}}\,\mathbf{E}_1(t-\tau_2)\,e^{i\mathbf{k}_1\cdot\mathbf{r}}$	$\mathbf{k}_s = 2\mathbf{k}_1$
$\mathbf{E}_1(t-\tau_1)\,e^{i\mathbf{k}_1\cdot\mathbf{r}}\,\mathbf{E}_2(t-\tau_2)\,e^{i\mathbf{k}_2\cdot\mathbf{r}}$	$\mathbf{k}_s = \mathbf{k}_1 + \mathbf{k}_2$
$\mathbf{E}_1^*(t-\tau_1)\,e^{-i\mathbf{k}_1\cdot\mathbf{r}}\,\mathbf{E}_1(t-\tau_2)\,e^{i\mathbf{k}_1\cdot\mathbf{r}}$	$\mathbf{k}_s = 0$
$\mathbf{E}_1^*(t-\tau_1)\,e^{-i\mathbf{k}_1\cdot\mathbf{r}}\,\mathbf{E}_2(t-\tau_2)\,e^{i\mathbf{k}_2\cdot\mathbf{r}}$	$\mathbf{k}_s = -\mathbf{k}_1 + \mathbf{k}_2$
$\mathbf{E}_2(t-\tau_1)\,e^{i\mathbf{k}_2\cdot\mathbf{r}}\,\mathbf{E}_1(t-\tau_2)\,e^{i\mathbf{k}_1\cdot\mathbf{r}}$	$\mathbf{k}_s = \mathbf{k}_1 + \mathbf{k}_2$
$\mathbf{E}_2(t-\tau_1)\,e^{i\mathbf{k}_2\cdot\mathbf{r}}\,\mathbf{E}_2(t-\tau_2)\,e^{i\mathbf{k}_2\cdot\mathbf{r}}$	$\mathbf{k}_s = 2\mathbf{k}_2$
$\mathbf{E}_2^*(t-\tau_1)\,e^{-i\mathbf{k}_2\cdot\mathbf{r}}\,\mathbf{E}_1(t-\tau_2)\,e^{i\mathbf{k}_1\cdot\mathbf{r}}$	$\mathbf{k}_s = \mathbf{k}_1 - \mathbf{k}_2$
$\mathbf{E}_2^*(t-\tau_1)\,e^{-i\mathbf{k}_2\cdot\mathbf{r}}\,\mathbf{E}_2(t-\tau_2)\,e^{i\mathbf{k}_2\cdot\mathbf{r}}$	$\mathbf{k}_s = 0$
$\mathbf{E}_1(t-\tau_1)\,e^{\mathbf{k}_1\cdot\mathbf{r}}\,\mathbf{E}_1^*(t-\tau_2)\,e^{-i\mathbf{k}_1\cdot\mathbf{r}}$	$\mathbf{k}_s = 0$
$\mathbf{E}_1(t-\tau_1)\,e^{\mathbf{k}_1\cdot\mathbf{r}}\,\mathbf{E}_2^*(t-\tau_2)\,e^{-i\mathbf{k}_2\cdot\mathbf{r}}$	$\mathbf{k}_s = \mathbf{k}_1 - \mathbf{k}_2$
$\mathbf{E}_1^*(t-\tau_1)\,e^{-i\mathbf{k}_1\cdot\mathbf{r}}\,\mathbf{E}_1^*(t-\tau_2)\,e^{-i\mathbf{k}_1\cdot\mathbf{r}}$	$\mathbf{k}_s = -2\mathbf{k}_1$
$\mathbf{E}_1^*(t-\tau_1)\,e^{-i\mathbf{k}_1\cdot\mathbf{r}}\,\mathbf{E}_2^*(t-\tau_2)\,e^{-i\mathbf{k}_2\cdot\mathbf{r}}$	$\mathbf{k}_s = -\mathbf{k}_1 - \mathbf{k}_2$
$\mathbf{E}_2(t-\tau_1)\,e^{i\mathbf{k}_2\cdot\mathbf{r}}\,\mathbf{E}_1^*(t-\tau_2)\,e^{-i\mathbf{k}_1\cdot r}$	$\mathbf{k}_s = -\mathbf{k}_1 + \mathbf{k}_2$
$\mathbf{E}_2(t-\tau_1)\,e^{i\mathbf{k}_2\cdot\mathbf{r}}\,\mathbf{E}_2^*(t-\tau_2)\,e^{-i\mathbf{k}_2\cdot\mathbf{r}}$	$\mathbf{k}_s = 0$
$\mathbf{E}_2^*(t-\tau_1)\,e^{-i\mathbf{k}_2\cdot\mathbf{r}}\,\mathbf{E}_1^*(t-\tau_2)\,e^{-i\mathbf{k}_1\cdot\mathbf{r}}$	$\mathbf{k}_s = -\mathbf{k}_1 - \mathbf{k}_2$
$\mathbf{E}_2^*(t-\tau_1)\,e^{-i\mathbf{k}_2\cdot\mathbf{r}}\,\mathbf{E}_2^*(t-\tau_2)\,e^{-i\mathbf{k}_2\cdot\mathbf{r}}$	$\mathbf{k}_s = -2\mathbf{k}_2$

$$\mathbf{E}(\mathbf{r}, t-\tau_1) = \mathbf{E}_1(t-\tau_1)\,e^{i\mathbf{k}_1\cdot\mathbf{r}} + \mathbf{E}_1^*(t-\tau_1)\,e^{-i\mathbf{k}_1\cdot\mathbf{r}} + \mathbf{E}_2(t-\tau_1)\,e^{i\mathbf{k}_2\cdot\mathbf{r}} + \mathbf{E}_2^*(t-\tau_1)\,e^{-i\mathbf{k}_2\cdot\mathbf{r}} \quad (57)$$

$$\mathbf{E}(\mathbf{r}, t-\tau_2) = \mathbf{E}_1(t-\tau_2)\,e^{i\mathbf{k}_1\cdot\mathbf{r}} + \mathbf{E}_1^*(t-\tau_2)\,e^{-i\mathbf{k}_1\cdot\mathbf{r}} + \mathbf{E}_2(t-\tau_2)\,e^{i\mathbf{k}_2\cdot\mathbf{r}} + \mathbf{E}_2^*(t-\tau_2)\,e^{-i\mathbf{k}_2\cdot\mathbf{r}} \quad (58)$$

12. References

(1) Perry, A.; Ahlborn, H.; Moore, P.; Space, B. *J. Chem. Phys.* **2003**, *118*, 8411.
(2) Perry, A.; Neipert, C.; Ridley, C.; Space, B. *Phys. Rev. E* **2005**, *71*, 050601(1).
(3) Perry, A.; Neipert, C.; Ridley, C.; Green, T.; Moore, P.; Space, B. *J. Chem. Phys.* Accepted for publication.
(4) Morita, A.; Hynes, J. T. *J. Phys. Chem. B* **2002**, *106*, 673.
(5) Morita, A.; Hynes, J. T. *Chem. Phys.* **2000**, *258*, 371.
(6) Pouthier, V.; Hoang, P.; Girardet, C. *J. Chem. Phys.* **1999**, *110*, 6963.
(7) Kuo, I. W.; Mundy, C. J. *Science* **2004**, *303*, 658.
(8) Vassilev, P.; Hartnig, C.; Koper, M. T.; Frechard, F.; van Santen, R. A. *J. Chem. Phys.* **2001**, *115*, 9815.
(9) Benjamin, I. *Phys. Rev. Lett.* **1994**, *73*, 2083.
(10) Taylor, R. S.; Dang, L. X.; Garrett, B. C. *J. Phys. Chem.* **1996**, *100*, 11720.
(11) Brown, E. C.; Mucha, M.; Jungwirth, P.; Tobias, D. J. *J. Phys. Chem. B* **2005**, *109*, 7934.
(12) Brown, M. G.; Walker, D. S.; Raymond, E. A.; Richmond, G. L. *J. Phys. Chem. B* **2003**, *107*, 237.
(13) Morita, A. *Chem. Phys. Lett.* **2004**, *398*, 361.
(14) Wei, X.; Shen, Y. R. *Phys. Rev. Lett.* **2001**, *86*, 4799.
(15) Pouthier, V.; Ramseyer, C.; Girardet, C. *J. Chem. Phys.* **1998**, *108*, 6502.
(16) Ostroverkhov, V.; Waychunas, G. A.; Shen, Y. R. *Phys. Rev. Lett.* **2005**, *94*, 0461021.
(17) Hore, D. K.; Hamamoto, M. Y.; Richmond, G. *J. Chem. Phys.* **2004**, *121*, 12589.
(18) Mucha, M.; Frigato, T.; Levering, L. M.; Allen, H. C.; Tobias, D. J.; Dang, L. X.; Jungwirth, P. *J. Phys. Chem. B* **2005**, *109*, 7617.
(19) Raymond, E. A.; Tarbuck, T. L.; Richmond, G. L. *J. Phys. Chem. B* **2002**, *106*, 2817.
(20) Shen, Y. *Solid State Commun.* **1998**, *108*, 399.
(21) Richmond, G. *Annu. Rev. Phys. Chem.* **2001**, *52*, 357.
(22) Richmond, G. *Chem. Rev.* **2002**, *102*, 2693.
(23) Gragson, D. E.; Richmond, G. L. *J. Phys. Chem. B* **1998**, *102*, 569.
(24) Shen, Y. *Principles of Nonlinear Optics*; Wiley: New York, 1984.
(25) Du, Q.; Superfine, R.; Freysz, E.; Shen, Y. *Phys. Rev. Lett.* **1993**, *70*, 2313.
(26) Raduge, C.; Pflumio, V.; Shen, Y. *Chem. Phys. Lett.* **1997**, *274*, 140.
(27) Shen, Y. R. *Proc. Natl. Acad. Sci. U.S.A.* **1996**, *93*, 12104.
(28) Freysz, E.; Du, Q.; Shen, Y. R. *Ann. Phys.* **1994**, *19*, 95.
(29) Du, Q.; Freysz, E.; Shen, Y. *Science* **1994**, *264*, 826.
(30) Superfine, R.; Huang, J. Y.; Shen, Y. R. *Phys. Rev. Lett.* **1991**, *66*, 1066.
(31) Gragson, D.; Richmond, G. *J. Chem. Phys.* **1997**, *107*, 9687.

(32) Brown, M. G.; Raymond, E. A.; Allen, H. C.; Scatena, L. F.; Richmond, G. L. *J. Phys. Chem. A* **2000**, *104*, 10220.
(33) Gragson, D. E.; Richmond, G. L. *J. Phys. Chem. B* **1998**, *102*, 3847.
(34) Gragson, D. E.; Richmond, G. L. *J. Am. Chem. Soc.* **1998**, *120*, 366.
(35) Scatena, L. F.; Brown, M. G.; Richmond, G. L. *Science* **2001**, *292*, 908.
(36) Baldelli, S.; Schnitzer, C.; Shultz, M. J.; Campbell, D. J. *J. Phys. Chem. B* **1997**, *101*, 10435.
(37) Baldelli, S.; Schnitzer, C.; Shultz, M. J.; Campbell, D. J. *Chem. Phys. Lett.* **1998**, *287*, 143.
(38) Shultz, M. J.; Schnitzer, C.; Simonelli, D.; Baldelli, S. *Int. Rev. Phys. Chem.* **2000**, *19*, 123.
(39) Schnitzer, C.; Baldelli, S.; Shultz, M. *J. Phys. Chem. B* **2000**, *104*, 585.
(40) Zhang, D.; Gutow, J.; Eisenthal, K. *J. Phys. Chem.* **1994**, *98*, 13729.
(41) Zhang, D.; Gutow, J.; Eisenthal, K. B. *J. Chem. Soc., Faraday* **1996**, *92*, 539.
(42) Wilson, K. R.; Cavalleri, M.; Rude, B. S.; Schaller, R. D.; Nilsson, A.; Pettersson, L. M.; Goldman, N.; Catalano, T.; Bozek, J.; Saykally, R. J. *J. Phys.: Condens. Matter* **2002**, *14*, L221.
(43) Wilson, K. R.; Schaller, R. D.; Co, D. T.; Saykally, R. J.; Rude, B. S.; Catalano, T.; Bozek, J. *J. Chem. Phys.* **2002**, *117*, 7738.
(44) Held, H.; Lvovsky, A. I.; Wei, X.; Shen, Y. R. *Phys. Rev. B* **2002**, *66*, 2051101.
(45) Wei, X.; Hong, S.-C.; Lvovsky, A. I.; Held, H.; Shen, Y. R. *J. Phys. Chem. B* **2000**, *104*, 3349.
(46) Bonn, M.; Ueba, H.; Wolf, M. *J. Phys.: Condens. Matter* **2005**, *17*, S201.
(47) Bordenyuk, A. N.; Benderskii, A. V. *J. Chem. Phys.* **2005**, *122*, 134713(1).
(48) Roke, S.; Kleyn, A. W.; Bonn, M. *Chem. Phys. Lett.* **2003**, *370*, 227.
(49) Voges, A.; Al-Abadleh, H.; Musorrafiti, M.; Bertin, P.; Nguyen, S.; Geiger, F. *J. Phys. Chem B* **2004**, *108*, 18675.
(50) Guyot-Sionnest, P.; Chen, W.; Shen, Y. *Phys. Rev. B* **1986**, *33*, 8254.
(51) Hommel, E. L.; Merle, J. K.; Ma, G.; Hadad, C. M.; Allen, H. C. *J. Phys. Chem. B* **2005**, *109*, 811.
(52) Hore, D.; King, J.; Moore, F.; Alavi, D.; Hamamoto, M.; Richmond, G. L. *Appl. Spectrosc.* **2004**, *58*, 1377.
(53) Schnitzer, C.; Baldelli, S.; Campbell, D. J.; Shultz, M. J. *J. Phys. Chem. A* **1999**, *103*, 6383.
(54) Kubo, R. A stochastic theory of line-shape and relaxation. In *Fluctuation, Relaxation and Resonance in Magnetic Systems*; Haar, D. T., Ed.; Oliver and Boyd: Edinburgh and London, 1961.
(55) Mukamel, S. *Principles of Nonlinear Optical Spectroscopy*; Oxford University Press: Oxford, 1995.
(56) Ueba, H. *Prog. Surf. Sci.* **1997**, *55*, 115.
(57) Boyd, R. W. *Nonlinear Optics*; Academic Press: London, 2003.
(58) Raschke, M. B.; Hayashi, M.; Lin, S. H.; Shen, Y. R. *Chem. Phys. Lett.* **2002**, *359*, 367.
(59) Hayashi, M.; Lin, S. H.; Shen, Y. R. *J. Phys. Chem. A* **2004**, *108*, 8058.
(60) Bloembergen, N.; Pershan, P. *Phys. Rev.* **1962**, *128*, 606.
(61) Venkatramani, R.; Mukamel, S. *J. Phys. Chem. B* **2005**, *109*, 8132.
(62) Tadjeddine, A.; Le Rille, A.; Pluchery, O.; Vidal, F.; Zheng, W. Q.; Peremans, A. *Phys. Status Solidi A* **1999**, *175*, 89.
(63) Vidal, F.; Tadjeddine, A. *Rep. Prog. Phys.* **2005**, *68*, 1095.
(64) Tadjeddine, A.; Le Rille, A. *Electrochim. Acta* **1999**, *45*, 601.
(65) Silbey, R.; Koedijk, J.; Völker, S. *J. Chem. Phys.* **1996**, *105*, 901.
(66) Mukamel, S. *Principles of Nonlinear Optical Spectroscopy*; Oxford University Press: Oxford, 1995; see Chapter 5, specifically p 129.
(67) Asbury, J. B.; Steinel, T.; Stromberg, C.; Corcelli, S. A.; Lawrence, C. P.; Skinner, J. L.; Fayer, M. D. *J. Phys. Chem A* **2004**, *108*, 1107.
(68) Bonvalet, A.; Nagle, J.; Berger, V.; Migus, A.; Martin, J.; Joffre, M. *Phys. Rev. Lett.* **1996**, *76*, 4392.
(69) Wei, X.; Miranda, P. B.; Zhang, C.; Shen, Y. R. *Phys. Rev. B* **2002**, *66*, 085401(1).
(70) Butcher, P.; Cotter, D. *The Elements of Nonlinear Optics*; Cambridge University Press: Cambridge, 1990.
(71) Mukamel, S.; Abramavicius, D. *Chem. Rev.* **2004**, *104*, 2073.
(72) Khalil, M.; Demirdoven, N.; Tokmakoff, A. *J. Phys. Chem. A* **2003**, *107*, 5258.
(73) Park, K.; Cho, M. *J. Chem. Phys.* **1998**, *109*, 10559.
(74) Shen, Y. R. *Annu. Rev. Phys. Chem.* **1989**, *40*, 327.
(75) Heinz, T. F. Second-order nonlinear optical effects at surfaces and interfaces. In *Nonlinear Surface Electromagnetic Phenomena*; Ponath, I., Stegeman, G., Eds.; Elsevier: Amsterdam, 1991.
(76) Heinz, G. A. R. T. F. Second-order nonlinear optical effects at surfaces and interfaces: Recent advances. In *Photonic Probes of Surfaces*; Ponath, I., Stegeman, G., Eds.; Elsevier: Amsterdam, 1995.
(77) Hirose, C.; Akamatsu, N.; Domen, K. *Appl. Spectrosc.* **1992**, *46*, 1051.
(78) Zhuang, X.; Miranda, P. B.; Kim, D.; Shen, Y. R. *Phys. Rev. B* **1999**, *59*, 12632.
(79) Byer, R. Parametric oscillators and nonlinear materials. In *Nonlinear Optics*; Harper, P., Wherritt, B., Eds.; Academic Press: London, 1977.
(80) Sauter, E. *Nonlinear Optics*; Wiley-Interscience: New York, 1996.
(81) Yeh, Y. L.; Zhang, C.; Held, H.; Mebel, A.; Wei, X.; Lin, S.; Shen, Y. R. *J. Chem. Phys.* **2001**, *114*, 1837.
(82) Lobau, J.; Wolfrum, K. *J. Opt. Soc. Am. B* **1997**, *14*, 2505.
(83) Lu, R.; Gan, W.; Hua Wu, B.; Chen, H.; Fei Wang, H. *J. Phys. Chem. B* **2004**, *108*, 7297.
(84) Wang, J.; Chen, C.; Buck, S.; Chen, Z. *J. Phys. Chem. B* **2001**, *105*, 12118.
(85) Guyot-Sionnest, P.; Shen, Y. *Phys. Rev. B* **1988**, *38*, 7985.
(86) Wang, J.; Clarke, M.; Chen, Z. *Anal. Chem.* **2004**, *76*, 2159.
(87) Wei, X.; Hong, X.; Zhuang, X.; Goto, T.; Shen, Y. *Phys. Rev. E* **2000**, *62*, 5160.
(88) Dick, B.; Gierulski, A.; Marowsky, G.; Reider, G. A. *Appl. Phys. B* **1985**, *38*, 107.
(89) Higgins, D. A.; Byerly, S. K.; Abrams, M. B.; Corn, R. M. *J. Phys. Chem.* **1991**, *95*, 6984.
(90) Wang, J.; Even, M.; Chen, X.; Schmaier, A.; Waite, J.; Chen, Z. *J. Am. Chem. Soc.* **2003**, *125*, 9914.
(91) Schweighofer, K. J.; Essmann, U.; Berkowitz, M. *J. Phys. Chem. B* **1997**, *101*, 3793.
(92) Dominguez, H.; Smondyrev, A. M.; Berkowitz, M. L. *J. Phys. Chem. B* **1999**, *103*, 9582.
(93) Chang, T.-M.; Dang, L. X. *J. Chem. Phys.* **1996**, *104*, 6772.
(94) Ducuing, J. Microscopic and macroscopic nonlinear optics. In *Nonlinear Optics*; Harper, P., Wherritt, B., Eds.; Academic Press: London, 1977.
(95) Heitler, W. *The Quantum Theory of Radiation*; Dover Publications Inc.: New York, 1984.
(96) McQuarrie, D. A. *Statistical Mechanics*; Harper and Row: New York, 1976.
(97) Gordon, R. G. Correlation functions for molecular motion. In *Advances in Magnetic Resonance*; Waugh, J. S., Ed.; Academic Press: New York and London, 1968.
(98) Kubo, R. Some aspects of the statistical-mechanical theory of irreversible processes. In *Lectures in Theoretical Physics*; Britton, W., Dunham, L., Eds.; Interscience Publishers Inc.: New York, 1959.
(99) Berne, B. J.; Harp, G. D. *Adv. Chem. Phys.* **1970**, *17*, 63.
(100) Ahlborn, H.; Ji, X.; Space, B.; Moore, P. B. *J. Chem. Phys.* **1999**, *111*, 10622; see discussion and references within.
(101) Moore, P.; Ahlborn, H.; Space, B. A combined time correlation function and instantaneous normal mode investigation of liquid-state vibrational spectroscopy. In *Liquid Dynamics Experiment, Simulation and Theory*; Fayer, M. D., Fourkas, J. T., Eds.; ACS Symposium Series; American Chemical Society: Washington, DC, New York, 2002.
(102) Borysow, J.; Moraldi, M.; Frommhold, L. *Mol. Phys.* **1985**, *56*, 913.
(103) Egelstaff, P. A. *Adv. Phys.* **1962**, *11*, 203.
(104) Cho, M. *J. Chem. Phys.* **2001**, *115*, 4424.
(105) Poulsen, J.; Nyman, G.; Rossky, P. *J. Phys. Chem.* **2004**, *108*, 19799.
(106) Lawrence, C.; Nakayama, A.; Makri, N.; Skinner, J. *J. Chem. Phys.* **2004**, *120*, 6621.
(107) Kim, H.; Rossky, P. J. *J. Phys. Chem. B* **2002**, *106*, 8240.
(108) Braun, R.; Casson, B.; Bain, C.; van der Ham, E.; Vrehen, Q.; Eliel, E.; Briggs, A.; Davies, P. *J. Chem. Phys.* **1999**, *110*, 4634.
(109) Pluchery, O.; Tadjeddine, A. *J. Electroanal. Chem.* **2001**, *500*, 379.
(110) Chen, Z. Private communication, 2005.
(111) He, G.; Liu, S. *Physics of Nonlinear Optics*; World Scientific: Singapore, 1999.
(112) Wang, C. C.; Duminski, A. *Phys. Rev. Lett.* **1968**, *20*, 668.
(113) Sutherland, R. *Handbook of Nonlinear Optics*; Marcel Dekker: New York, 1996.
(114) Terhune, R.; Maker, P.; Savage, C. *Phys. Rev. Lett.* **1962**, *8*, 404.
(115) Bloembergen, N.; Chang, R.; Jha, S.; Lee, C. *Phys. Rev.* **1968** *174*, 813 and references within.
(116) Lee, C. H.; Chang, R. K.; Bloembergen, N. *Phys. Rev. Lett.* **1967**, *18*, 167.
(117) Maker, P. D.; Terhune, R. W. *Phys. Rev.* **1965**, *137*, A801.
(118) Zhao, X. L.; Ong, S.; Eisenthal, K. B. *Chem. Phys. Lett.* **1993**, *202*, 513.
(119) Gragson, D.; McCarty, B.; Richmond, G. L. *J. Phys. Chem.* **1996**, *100*, 14272.
(120) Wang, H. Second harmonic generation studies of chemistry at liquid interfaces. Thesis, Columbia University, 1996.
(121) Ong, S.; Zhao, X. L.; Eisenthal, K. B. *Chem. Phys. Lett.* **1992**, *191*, 327.
(122) Raymond, E. A.; Tarbuck, T. L.; Brown, M. G.; Richmond, G. L. *J. Phys. Chem. B* **2003**, *107*, 546.
(123) DeVane, R.; Space, B.; Perry, A.; Neipert, C.; Ridley, C.; Keyes, T. *J. Chem. Phys.* **2004**, *121*, 3688.

(124) Ahlborn, H.; Ji, X.; Space, B.; Moore, P. B. *J. Chem. Phys.* **1999**, *111*, 10622.
(125) Ahlborn, H.; Ji, X.; Space, B.; Moore, P. B. *J. Chem. Phys.* **2000**, *112*, 8083.
(126) Moller, K. B.; Rey, R.; Hynes, J. T. *J. Phys. Chem. A* **2004**, *108*, 1275.
(127) Lawrence, C. P.; Skinner, J. L. *J. Chem. Phys.* **2003**, *118*, 264.
(128) Lawrence, C. P.; Skinner, J. L. *J. Chem. Phys.* **2002**, *117*, 8847.
(129) Reimers, J. R.; Watts, R. O. *Chem. Phys.* **1984**, *91*, 201.
(130) Reimers, J.; Watts, R. *Chem. Phys. Lett.* **1983**, *94*, 222.
(131) Reimers, J.; Watts, R. *Mol. Phys.* **1986**, *57*, 777.
(132) Toukan, K.; Rahman, A. *Phys. Rev. B* **1985**, *31*, 2643.
(133) Zhu, S.-B.; Singh, S.; Robinson, G. W. *Water in Biology, Chemistry and Physics*; World Scientific: New Jersey, 1996; see the refrences within.
(134) Raymond, E. A.; Richmond, G. L. *J. Phys. Chem. B* **2004**, *108*, 5051.
(135) Bertie, J. E.; Eysel, H. H. *Appl. Spectrosc.* **1985**, *39*, 392.
(136) Bertie, J. E.; Lan, Z. *Appl. Spectrosc.* **1996**, *50*, 1047.
(137) Ji, X.; Ahlborn, H.; Moore, P.; Space, B. *J. Chem. Phys.* **2000**, *113*, 8693.
(138) Shah, V.; Bowen, F.; Space, B. *J. Chem. Phys.* **2000**, *112*, 10998.
(139) Ji, X.; Ahlborn, H.; Space, B.; Moore, P.; Zhou, Y.; Constantine, S.; Ziegler, L. D. *J. Chem. Phys.* **2000**, *112*, 4186.
(140) Moore, P.; Space, B. *J. Chem. Phys.* **1997**, *107*, 5635.
(141) Moore, P. B.; Ji, X.; Ahlborn, H.; Space, B. *Chem. Phys. Lett.* **1998**, *296*, 259.
(142) Space, B.; Rabitz, H.; Lõrincz, A.; Moore, P. *J. Chem. Phys.* **1996**, *105*, 9515.
(143) Keyes, T.; Fourkas, J. T. *J. Chem. Phys.* **2000**, *112*, 287.
(144) Murry, R. L.; Fourkas, J. T.; Li, W.-X.; Keyes, T. *Phys. Rev. Lett.* **1999**, *83*, 3550.
(145) Ribeiro, M.; Wilson, M.; Madden, P. *J. Chem. Phys.* **1999**, *110*, 4803.
(146) Kindt, J. T.; Schmuttenmaer, C. A. *J. Chem. Phys.* **1997**, *106*, 4389.
(147) Keyes, T. *J. Chem. Phys.* **1997**, *106*, 46.
(148) Keyes, T. *J. Chem. Phys.* **1996**, *104*, 9349.
(149) Murry, R. L.; Fourkas, J. T.; Keyes, T. *J. Chem. Phys.* **1998**, *109*, 2814.
(150) Kindt, J. T.; Schmuttenmaer, C. A. *J. Chem. Phys.* **1999**, *110*, 8589.
(151) Berne, B. J.; Pecora, R. *Dynamic Light Scattering*; Robert E. Kroeger Publishing Company: Malabar, Florida, 1990.
(152) In our previous paper (ref 1), we accidentally showed the harmonic quantum correction factor appropriate for the whole correlation function $C(\omega) = C_{Cl}(\omega)(\beta \bar{h} \omega/(1 - e^{-\beta\hbar\omega})$ instead of the correction for the real part, $C_R(\omega)$, given here. Note that in the high frequency limit the two factors only differ by a factor of 2.
(153) Allen, M. P.; Tildesley, D. J. *Computer Simulation of Liquids*; Clarendon Press: Oxford, 1989.
(154) Bode, K. A.; Applequist, J. *J. Phys. Chem.* **1996**, *100*, 17820.
(155) Applequist, J.; Quicksall, C. O. *J. Chem. Phys.* **1977**, *66*, 3455.
(156) Applequist, J.; Carl, J. R.; Fung, K.-K. *J. Am. Chem. Soc.* **1972**, *94*, 2952.
(157) Thole, B. *Chem. Phys.* **1981**, *59*, 341.
(158) Avila, G.; Fernandez, J.; Mate, B.; Tejeda, G.; Montero, S. *J. Mol. Spectrosc.* **1999**, *196*, 77.
(159) Amos, R. D. *Adv. Chem. Phys.* **1987**, *67*, 99.
(160) Vrbka, L.; Mucha, M.; Minofar, B.; Jungwirth, P.; Brown, E. C.; Tobias, D. J. *Curr. Opin. Colloid Interface Sci.* **2004**, *9*, 67.
(161) Knipping, E. M.; Lakin, M. J.; Foster, K. L.; Jungwirth, P.; Tobias, D. J.; Gerber, R. B.; Dabdub, D.; Finlayson-Pitts, B. J. *Science* **2000**, *288*, 301.
(162) Jungwirth, P.; Tobias, D. J. *J. Phys. Chem. B* **2000**, *104*, 7702.
(163) Onsager, L.; Samaras, N. N. T. *J. Chem. Phys.* **1934**, *2*, 528.
(164) Heydweiller, A. *Ann. Phys.* **1910**, *33*, 145.
(165) Roeselova, M.; Vieceli, J.; Dang, L. X.; Garrett, B. C.; Tobias, D. J. *J. Am. Chem. Soc.* **2004**, *126*, 16308.
(166) Jungwirth, P.; Tobias, D. J. *J. Phys. Chem. B* **2001**, *105*, 10468.
(167) Petersen, P. B.; Saykally, R. J. *Chem. Phys. Lett.* **2004**, *397*, 51.
(168) Liu, D. F.; Ma, G.; Levering, L. M.; Allen, H. C. *J. Phys. Chem. B* **2004**, *108*, 2252.
(169) Ghosal, S.; Hemminger, J.; Bluhm, H.; Mun, B.; Hebenstreit, E.; Ketteler, G.; Ogletree, D.; Requejo, F.; Salmeron, M. *Science* **2005**, *307*, 563.
(170) Guyot-Sionnest, P. *Phys. Rev. Lett.* **1991**, *66*, 1489.
(171) Cho, M. *PhysChemComm* **2002**, *5*, 40.
(172) Fujiyoshi, S.; aki Ishibashi, T.; Onishi, H. *J. Phys. Chem. B* **2004**, *108*, 10635.
(173) Shen, Y. *J. Sel. Top. Quantum Elec.* **2000**, *6* (6), 1375.
(174) Shen, Y. *Pure Appl. Chem.* **2001**, *73*, 1589.
(175) Corn, R. M.; Higgins, D. A. *Chem. Rev.* **1994**, *94*, 107.
(176) Eisenthal, K. *Chem. Rev.* **1996**, *96*, 1343.

CR040379Y